International Journal of Hydrogen Energy 265 (2026) 156980

Contents lists available at ScienceDirect

International Journal of Hydrogen Energy

journal homepage: www.elsevier.com/locate/he

Non-isothermal reduction of TeO_2 by hydrogen: Integrated distributed-activation-energy-model (DAEM)-shrinking-core-model (SCM) kinetic modeling and enthalpy-entropy compensation analysis

Hanwen Chung [a,*,1], Bojan Janković [b,1], Semiramis Friedrich [a], Bernd Friedrich [a]

[a] IME Process Metallurgy and Metal Recycling, RWTH Aachen University, Aachen, 52072, Germany
[b] University of Belgrade, "Vinča" Institute of Nuclear Sciences - National Institute of the Republic of Serbia, Mike Petrovića Alasa 12-14, P.O. Box 522, Belgrade, 11001, Serbia

ARTICLE INFO

Keywords:
Hydrogen reduction kinetics
Non-isothermal thermogravimetry
DAEM-SCM modeling
Diffusion
Enthalpy-entropy compensation
Van't hoff analysis

ABSTRACT

The non-isothermal reduction of TeO_2 (tellurium dioxide) by hydrogen (H_2) was investigated using thermal analysis (TG/DTG) techniques at multiple heating rates (1.0, 4.8, 9.6, and 18.8 K/min). Reaction kinetics were evaluated through an integrated Distributed Activation Energy Model (DAEM) coupled with a Shrinking Core Model (SCM), enabling accurate description of the multi-step gas-solid process. The results reveal a pronounced variation of the apparent activation energy with conversion, indicating a transition from surface-controlled to diffusion-limited regimes. Analysis of ln*P* *vs.* 1/*T* relationship shows the significant deviation from linearity, confirming non-ideal Van't Hoff behavior and the presence of enthalpy-entropy compensation (EEC). The compensation temperature ($T_{comp} \approx 847$ K) and Compensation Quality Factor ($CQF = 0.640$) suggest a physically meaningful but non-isokinetic process. High-temperature regions exhibit elevated apparent enthalpy values, consistent with the product-layer diffusion control. The combined kinetic-thermodynamic approach provides comprehensive insight into the mechanism of TeO_2 reduction by hydrogen.

Nomenclature

Abbreviations

TG – Thermogravimetry
DTG - Derivative thermogravimetry
DAEM - Distributed Activation Energy Model
SCM - Shrinking Core Model
EEC - Enthalpy-entropy compensation
XRD - X-ray diffraction
TA - Thermal analysis
DAEM-SCM – Distributed activation energy model/shrinking core model
FR - Friedman's method (isoconversional)
NMO - Numerical optimization (isoconversional)
TCE - Thermodynamic compensation effect
TG-DTG – Thermogravimetry – Derivative thermogravimetry
RMSE - The root mean square error
AIC - Akaike information criterion
DAEM + SCM – Hybrid distributed activation energy –shrinking core modeling
FWO – Flynn-Wall-Ozawa (model-free method)
CQF – Compensation Quality Factor

w_i – the *i*-th component weight (contribution) (expressed in (%))
A_i – pre-exponential factor related to *i*-th component (s^{-1})
$g(\alpha)$ – the integral reaction model
k_β – the effective diffusion rate constant related to the considered heating rate (min^{-1})
$E_{a,d}$ – the diffusion activation energy (kJ/mol)
A_d – the diffusion pre-exponential factor (s^{-1})
T_d – the diffusion onset temperature (^oC)
$E_{a,DAEM}$ – the activation energy from DAEM component (heterogeneous kinetics) (kJ/mol)
$E_{a,SCM}$ – the activation energy from SCM component (product-layer diffusion) (kJ/mol)
w - the fractional contribution of the kinetically controlled regime (–)
k – the rate constant (s^{-1})
$\alpha(T)$ – Conversion – temperature reduction curve (experimental)
$\Delta H^{\#}$ – activation enthalpy (kJ/mol)
$\Delta S^{\#}$ – activation entropy (J/(mol K))
$\Delta G^{\#}$ – Gibb's free energy of activation (kJ/mol)
$\Delta G^{\#}_{comp}$ – the free energy of compensation (J/mol)
T_{exp} – the average experimental temperatures at multiple heating rates (K)
T_{comp} – the compensation temperature (K)
T_{hm} – the harmonic mean temperature (K)

(*continued on next column*)
(*continued*)
(*continued on next page*)

* Corresponding author.
E-mail address: hchung@metallurgie.rwth-aachen.de (H. Chung).
[1] These authors contributed equally to this work.

https://doi.org/10.1016/j.ijhydene.2026.156980
Received 24 June 2026; Received in revised form 27 July 2026; Accepted 6 August 2026
Available online 8 August 2026
0360-3199/© 2026 The Authors. Published by Elsevier Ltd on behalf of Hydrogen Energy Publications LLC. This is an open access article under the CC BY license (http://creativecommons.org/licenses/by/4.0/).

(*continued*)

CI/CL – Confidence interval (95 %)/ Confidence level (95/99 %)

Physical/Chemical Quantities

T – temperature (^{o}C or K)

T_o – initial temperature at the start of experiment (^{o}C or K)

t – the time (s or min)

Δm – the mass loss (%)

Δm_{total} – the total mass loss (%)

$\Delta m_{theoretical}$ – the theoretical mass loss (%)

$m_{residual}$ – the residual mass (%)

dm/dt – the mass loss rate (%/min)

T_p – the maximum (peak) DTG – curve temperature (^{o}C)

$E_a(\alpha)$ - Conversion-dependent activation energy (apparent) (kJ/mol)

A_α - Conversion-dependent pre-exponential factor (apparent) (s^{-1})

E_a – the effective activation energy (kJ/mol)

$logA$ – the logarithm of effective pre-exponential factor

ΔE_a – the error (standard deviation) of effective activation energy (kJ/mol)

R^2 – the coefficient of determination

a – the compensation coefficient (s^{-1})

b – the compensation coefficient (mol·(kJ)$^{-1}$)

k_{iso} – the isokinetic rate constant (s^{-1})

T_{iso} – the isokinetic temperature (K [^{o}C])

R – the universal gas constant (8.314 J/(mol·K))

$f(E)$ – the activation energy distribution (mol·(kJ)$^{-1}$)

f_{total} – the total (complex/multi-component) activation energy distribution (mol·(kJ)$^{-1}$)

E_i – the i-th component activation energy (kJ/mol)

$t{\cdot}\sigma$ – product of Student's t-distribution value at significance level $\alpha = 0.05$, and standard error value for T_{comp} (K)

ln$P$ - the natural logarithm of equilibrium pressure (−)

N – the number of samples (statistical sample)

T_{low} – the lower-temperature limit (K)

T_{high} – the higher-temperature limit (K)

$[T_{low}, T_{high}]$ – the temperature interval which defines corresponding bounds in $1/T$-space (K)

$T_{\min}$ – the temperature at which ln$P$ reaches a local minimum (or inflection in slope behavior) (the temperature at which the smallest ln$P$ spread occurs) (K)

T^* – the characteristic temperature point, where the curvature changes in ln$P$-$1/T$ dependence plot (the temperature at which ln$P$ spread is the largest) (K)

ΔH_{app} - the apparent reaction enthalpy (kJ/mol)

Greek Letters

α – the conversion (−)

β – the heating rate (K/min)

γ – the confidence threshold

σ_i – the width ("breadth") of the i-th component activation energy distribution (kJ/mol)

σ – the dispersion parameter, related to the width of the activation energy distribution (kJ/mol)

φ – the hydrogen flow rate (mL/min)

1. Introduction

The growing global interest in hydrogen as a clean energy carrier has stimulated extensive research into hydrogen-based reduction processes, particularly for metal oxides and waste-derived materials [1]. Hydrogen-driven reactions offer significant advantages over conventional carbon-based reduction routes, including reduced greenhouse gas emissions and improved process controllability, making them highly attractive for sustainable materials processing and circular economy applications [2–4].

Tellurium dioxide (TeO_2) is an important functional material widely used in optical devices, semiconductor technologies, and thermoelectric systems [5,6]. Additionally, the increasing demand for tellurium in photovoltaic and electronic applications has intensified the need for efficient recovery and recycling strategies. Hydrogen reduction of TeO_2 represents a promising route for producing elemental tellurium; however, kinetic and the mechanistic aspects of this process remain insufficiently understood, particularly under non-isothermal conditions [7–10]. The use of hydrogen (H_2) as a reducing agent has gained significant attention due to its high reactivity, clean reaction pathway, and the absence of carbon-containing by-products [11–13]. In contrast to the conventional carbothermic reduction, hydrogen enables the conversion of metal oxides through the formation of water vapor as the sole gaseous product, thereby significantly reducing greenhouse gas emissions and environmental impact [14]. In the specific case of TeO_2, the hydrogen reduction represents an efficient and selective route for the production of elemental tellurium, particularly under non-isothermal (dynamic) conditions, where temperature-dependent kinetic behavior governs the overall process [15]. From a metallurgical perspective, the hydrogen-based reduction processes are increasingly recognized as key enabling technologies for sustainable metal extraction and recycling. Recent studies highlight the growing role of hydrogen metallurgy in processing critical and strategic elements, particularly within circular economy frameworks aimed at recovering valuable metals from secondary resources such as electronic waste and industrial residues [16–18]. In this context, the reduction of TeO_2 by H_2 is of the particular importance, as it enables controlled and selective transformation pathways. Non-isothermal kinetic analysis provides essential insights into reaction mechanisms, activation energy evolution, and the rate-controlling steps, thereby supporting improved reactor design and process optimization in hydrogen-based systems [19,20].

Thermogravimetry (TG) and derivative thermogravimetry (DTG) are powerful techniques for investigating gas-solid reactions, enabling real-time monitoring of mass changes and reaction rates as a function of temperature. These methods provide essential information on the reaction pathways, rate-controlling steps, and thermal stability, and have been widely applied in the study of reduction, oxidation, and decomposition processes [21,22]. In particular, the non-isothermal TG/DTG experiments conducted at the multiple heating rates, allow for detailed kinetic analysis using model-free (isoconversional) and model-based approaches. Model-free (isoconversional) methods are commonly employed to determine the apparent activation energy as a function of conversion without assuming a specific reaction model [23]. These methods are particularly useful for identifying changes in reaction mechanisms across different conversion ranges. However, they do not provide a direct description of the reaction pathway or enable reconstruction of the experimental TG and/or DTG curves. To overcome these limitations, the distributed activation energy model (DAEM) has been increasingly applied to describe the complex multi-step reactions. The DAEM assumes a continuous distribution of activation energies, allowing the representation of overlapping processes and heterogeneous reaction environments [24–26]. Nevertheless, the classical DAEM backgrounds may not fully capture diffusion-controlled phenomena, which are often observed in the gas-solid reduction systems at higher process progression levels [27–29]. In such cases, the shrinking core model (SCM) provides a physically meaningful framework for describing reactions involving the formation of a product layer around an unreacted core. Depending on the rate-limiting step, the SCM can account for chemical reaction control, diffusion through the product layer, or external mass transfer resistance [30–32]. The combination of DAEM and SCM therefore offers a comprehensive approach for modeling both kinetically controlled and the diffusion-limited stages of the reduction process.

Furthermore, thermodynamic analysis based on transition state theory enables deeper insight into the nature of the activated complex and the energetic landscape of the process of interest. In this context, the enthalpy-entropy compensation (EEC) effect [33], originally formulated within the framework of Henry Eyring's theory, provides evidence for a correlation between activation enthalpy and entropy, suggesting a common mechanistic origin arising from the isoconversional principle [34,35]. Hydrogen plays a critical role in the reduction kinetics of TeO_2 by providing a highly reactive, clean reducing environment that governs

the rate-controlling steps through H_2-solid interactions and water formation as the only by-product. In the non-isothermal conditions, the sensitivity of TeO_2 reduction kinetics to the temperature-dependent hydrogen diffusion and surface reaction processes makes hydrogen essential for accurately describing both the mechanism and activation energy evolution of the system. Since the hydrogen-driven reduction of TeO_2 provides a kinetically sensitive system in which the temperature-dependent H_2-solid interactions govern the apparent reaction rate, this makes it very suitable for detailed kinetic interpretation of the process. In this context, the model-free (isoconversional) analysis is essential to resolve the conversion-dependent activation energy profile, which subsequently serves as a basis for mechanistic formulation, using the SCM to describe diffusion-reaction control within the solid particle. Furthermore, the coupled evolution of enthalpy and entropy parameters during the hydrogen reduction often manifests as an enthalpy-entropy compensation (EEC) effect, reflecting an intrinsic thermodynamic-kinetic coupling of H_2-TeO_2 reaction pathway under the non-isothermal conditions.

Despite the considerable interest in hydrogen-based reduction of metal oxides and the increasing importance of tellurium-containing materials for advanced energy technologies, several important aspects of the TeO_2-H_2 reduction process remain insufficiently understood. The previous investigations have primarily focused on overall reduction behavior, the apparent kinetic parameters, and thermodynamic characteristics, while considerably less attention has been devoted to establishing a physically consistent relationship between intrinsic kinetic heterogeneity, particle-scale transport phenomena, and thermodynamic driving forces during the reduction process. In particular, the evolution of the reduction mechanism from chemically controlled to diffusion-influenced regimes has not been systematically interpreted within a unified kinetic framework capable of simultaneously accounting for distributed activation energies, progressive development of diffusion resistance, and thermodynamic compensation effects, respectively. Addressing these un-resolved issues is an essential for achieving a more comprehensive understanding of the hydrogen reduction mechanisms and for improving the predictive capability of the kinetic models used in the design and optimization of hydrogen-based metallurgical processes.

To address these knowledge gaps, the present study develops an integrated kinetic-thermodynamic framework for non-isothermal hydrogen reduction of TeO_2 by coupling the Distributed Activation Energy Model (DAEM), the Shrinking Core Model (SCM), and enthalpy-entropy compensation (EEC) analysis. So, the objective of this study is to enables the simultaneous interpretation of the intrinsic reaction kinetics, particle-scale diffusion effects, and thermodynamic compensation phenomena within a unified modeling framework, thereby providing new mechanistic insights into the hydrogen reduction behavior of TeO_2 and establishing a methodology that may be extended to other heterogeneous gas-solid reduction systems.

2. Materials and methods

2.1. Starting material

In this study, the starting material – precursor, introduced into the reduction course, was commercial tellurium dioxide (TeO_2) powder with purity of 99.99 wt % (4 N) (Manufacturer: Wuhan Tuocai Technology Co., Ltd., Wuhan, China), used without any further purification. This material is usually used in applications for high-end semiconductor materials, artificial crystals, solar cells, and the conductive pastes. The powders have particle sizes of $d_{10} = 3.05$ μm, $d_{50} = 7.830$ μm, and $d_{90} = 15.56$ μm, with the full particle size distribution shown in Fig. S0, Supplementary Material. The XRD (X-ray diffraction) analysis (Fig. S1, Supplementary Material) confirmed that the commercial TeO_2 powder (99.99 wt %) consists of a single tetragonal phase (paratellurite), with no detectable impurities. The sharp diffraction peaks indicate the high crystallinity, validating its suitability for kinetic studies of hydrogen reduction. The XRD test of the starting material was described in section S·I., within the Supplementary Material.

2.2. Reduction process in non-isothermal conditions monitored by TG-DTG measurements

To monitor the process of non-isothermal reduction of TeO_2 by H_2 through thermal analysis (TA), approximately 250 mg of the sample was placed in an alumina crucible, and heated from ambient temperature to 620 °C under flowing hydrogen (99.999 % purity), using simultaneous thermoanalyzer Netzsch STA 429 (Netzsch Gerätebau GmbH, Selb, Germany). The hydrogen flow rate was maintained at $\varphi = 79$ mL/min, throughout the experiments. An empty alumina crucible was used as the reference in order to minimize the temperature measurement deviation. The selected sample mass provided reproducible the mass loss profiles, while ensuring adequate signal-to-noise ratio for a subsequent kinetic analysis. The reduction measurements were carried out in the linear temperature-time program under non-isothermal conditions ($T = T_o + \beta \cdot t$, where T is the instantaneous temperature (°C or K), T_o is the initial temperature at the start of the experiment (°C or K), β is the heating rate (K/min), and t is the time), at four different heating rate of $\beta = 1.0$, 4.8, 9.6, and 18.8 K/min. Duplicate measurements were performed for each test to confirm reproducibility and repeatability of measurements. Upon the completion of the heating program, the hydrogen atmosphere was switched to an inert gas, and the sample was allowed to cool naturally.

2.3. Kinetic and thermodynamic analysis of TeO_2 reduction by hydrogen (H_2) - introduction of a novel hybrid DAEM-SCM modeling of the reduction process

A complete description of the kinetic and thermodynamic characteristics of the investigated reduction process, which includes applied methods and models, is presented in the Supplementary Material. Section S·II. presents the isoconversional (model-free) kinetic analysis of the reduction process through the application of differential Friedman's (FR) method and the numerical optimization (NMO) method. Further, section S·III. is referred to DAEM (Distributed activation energy model) analysis and distributed kinetics, while section S·IV. is referred to the application of shrinking core model (SCM) and diffusion-controlled regime description of considered process. Section S.V. (Supplementary Material) encompasses detail description of a novel hybrid DAEM-SCM modeling for TeO_2 reduction by H_2 (in order to improve parameter identifiability and to avoid heating-rate-dependent bias, all model parameters, including the weighting coefficient w, were optimized simultaneously using the complete set of thermo-analytical datasets acquired at all heating rates). Finally, section S·VI. shows methods used in thermodynamic analysis of reduction process, including the role of thermodynamic compensation effect (TCE) in a comprehensive understanding of the reduction mechanism of TeO_2 by hydrogen.

Under the above considerations, the present work aims to provide a comprehensive kinetic and thermodynamic investigation of the non-isothermal reduction of TeO_2 in a hydrogen atmosphere, where the specific objectives are the following: a) to experimentally characterize the reduction behavior of TeO_2 using simultaneous TG-DTG analysis at multiple heating rates, enabling the identification of distinct reaction stages, b) to apply the model-free (isoconversional) methods, including differential (Friedman) and numerical optimization approaches, in order to determine the conversion-dependent activation energy $E_a(\alpha)$ and assess the complexity of the reduction mechanism, c) to modeling the reduction kinetics using a novel introduced the hybrid DAEM-SCM framework, which successfully describes the reduction process in an entire conversion range (DAEM accounts for the kinetically controlled stages, while the SCM captures the diffusion-controlled regime), d) to evaluate the presence and significance of the enthalpy-entropy compensation (EEC) effect and the related thermodynamic

compensation phenomena, thereby providing insight into the transition state characteristics and mechanistic evolution of the process, and finally e) to establish a correlation between kinetic and thermodynamic parameters, contributing to a deeper understanding of interplay between reaction energetics and mechanism in heterogeneous reduction system.

3. Results and discussion

3.1. Simultaneous TG-DTG measurements of non-isothermal reduction of TeO_2 by hydrogen

Based on the initial structural state of the experimental specimen (from XRD pattern shown in Fig. S1, Supplementary Material), which confirms the presence of single-phase α-TeO_2 (paratellurite) (the high crystallinity, without impurities), the current material guarantees that all TG mass losses originate purely from reduction chemistry, but not by phase contamination. Fig. 1 shows the simultaneous TG-DTG curves of non-isothermal reduction process of TeO_2 by hydrogen, at the heating rate of $\beta = 4.8$ K/min.

The first stage (**1**) (Fig. 1) is characterized with very small mass loss (~0.11 %), and this is attributed to removal of physically adsorbed moisture (surface species), where no structural change in TeO_2 takes place. The actual stage can be described Eq. (1):

$$TeO_2xH_2O \xrightarrow{\Delta} TeO_2 + xH_2O. \quad (1)$$

The second stage (**2**) (Fig. 1) exhibits a slightly higher mass loss (~1.59 %) with increasing temperature, where observed stage represents initial phase of reduction process, whereby initial surface reduction begins. Within this stage, one can expect the formation of oxygen vacancies and the nucleation of reduced species. The stage (**2**) can most likely be described by the following equation:

$$TeO_2 + xH_2 \xrightarrow{\Delta} TeO_{2-x} + xH_2O. \quad (2)$$

The current stage is probably characterized by the surface-controlled reaction, with early nucleation regime.

At higher temperatures, stage (**3**) appears (Fig. 1), which is characterized by the largest mass loss of specimen (~13.36 %). This stage represents the main reduction stage, where the defined shape of the DTG peak positioned at about ≈ 500 °C, can be clearly seen. The main chemical reaction that describes this reduction step can be represented in the form:

$$TeO_2 + 2H_2 \xrightarrow{\Delta} Te + 2H_2O, \quad (3)$$

where it transforms into metallic tellurium (Te). Namely, the bulk reduction: $TeO_2 \rightarrow Te$ takes place approximately ~500 °C, which corresponds to DTG peak (Fig. 1). In this case, one might expect a mixed mechanism of reduction control to occur, involving interface reaction and the gas diffusion (H_2/H_2O) [36,37]. At temperatures corresponding to the DTG peak (associated with maximum reaction rate (Fig. 1)), the controlling mechanism often transitions to the mixed regime, where both processes contribute significantly to the overall kinetics [37].

With further progression in the temperature, the process enters into the stage (**4**) characterized by the mass loss of ~6.48 % (Fig. 1), which represents the final reduction of residual TeO_2 and where exists diffusion-limited regions (residual $TeO_2 \rightarrow Te$: diffusion-controlled completion). This stage can be characterized with property where the product layer (Te) limits the H_2 access. It should be noted that at ~500 °C where the DTG feature occurs (Fig. 1), the reaction rate is maximal and where, both, the reaction kinetics and transport processes are active. On the other hand, the formation of metallic Te creates barrier for the gas diffusion. So, simultaneous processes may take place, such as H_2 diffusion inward, H_2O diffusion outward, and the interface reaction at TeO_2/Te boundary. Therefore, the mixed control mechanism can be expected for the investigated experimental specimen used in this study.

From the profile of the obtained thermo-analytical curves (Fig. 1), TG/DTG monitoring identifies distinctly the reduction process temperature window, whereby, it is known that the process can start as early as at room temperature [9], but complete conversion in the solid state is achieved near the melting point of tellurium (≈450 °C). DTG profile is crucial for controlling the evaporation (volatilization) of metals, which manifests itself as the mass loss greater than the theoretical (over 20.05 %) (Fig. 1). Additionally, an increasing of hydrogen flow improves the kinetics by reducing diffusion resistance through the gas boundary layer around the particles. This is consistent with the DTG behavior, where a well-defined, the sharp maximum appears, and no excessive broadening or tailing at low temperatures takes place (Fig. 1).

Fig. 2 shows the set of the DTG curves recorded at the various heating rates ($\beta = 1.0$, 4.8, 9.6, and 18.8 K/min) for non-isothermal reduction process of TeO_2 by H_2.

The DTG curves recorded at heating rates of 1.0, 4.8, 9.6 and 18.8 K/min exhibit the characteristic features of non-isothermal gas-solid reduction processes. A systematic shift of the DTG peak temperature (T_p) toward higher values is observed with increasing heating rate (Fig. 2). This behavior arises from thermal lag and kinetic delay, as higher heating rates reduce the time available for the system to reach equilibrium at a given temperature, thereby requiring higher temperatures to achieve the same conversion [21,38]. In addition to the peak shift, the DTG curves become progressively broader and slightly asymmetric at the higher β (Fig. 2), indicating a widening of the effective reaction temperature interval [39]. This broadening reflects an increased overlap of elementary steps and the growing contribution of transport limitations, particularly at higher conversions [40,41]. Such behavior is

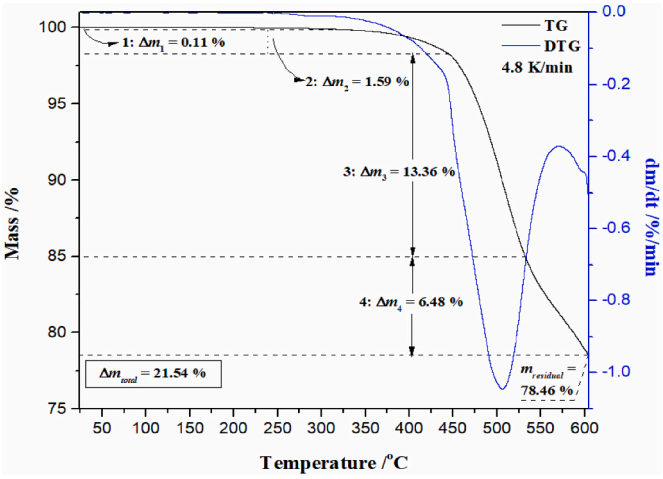


Fig. 1. Simultaneous TG-DTG curves of TeO_2 reduction under a hydrogen atmosphere at a heating rate of $\beta = 4.8$ K/min. The four distinct mass loss stages were identified: **1** – removal of adsorbed species ($\Delta m_1 = 0.11$ %), **2** – the initial surface reduction ($\Delta m_2 = 1.59$ %), **3** – the dominant bulk reduction of TeO_2 to Te ($\Delta m_3 = 13.36$ %), and **4** – the diffusion-controlled completion ($\Delta m_4 = 6.48$ %). The total mass loss ($\Delta m_{total} = 21.54$ %) agrees well with theoretical value for complete TeO_2 reduction, confirming the reaction pathway (*theoretical validation* – for reaction: $TeO_2 \rightarrow Te$, M(TeO_2) = 159.6 g/mol, M (Te) = 127.6 g/mol, $\Delta m_{theoretical} = 32/159.6 = 0.200501 \times 100\ \% \approx 20.05\ \%$; the obtained result of 21.54 % is slightly higher than theoretical, which can be explained by the presence of adsorbed species, experimental conditions, and maybe minor side reactions – slight excess of the measured mass loss over the theoretical value *is most likely* associated with minor volatilization of metallic tellurium at the highest temperatures, following its formation in the molten state (*melting point*: ~449.5 °C); however, the magnitude of this effect is small and does not influence on the overall interpretation of the reduction mechanism, or the subsequent kinetic analysis). The residual mass at T ~603.95 °C amounts $m_{residual} = 78.46$ %.

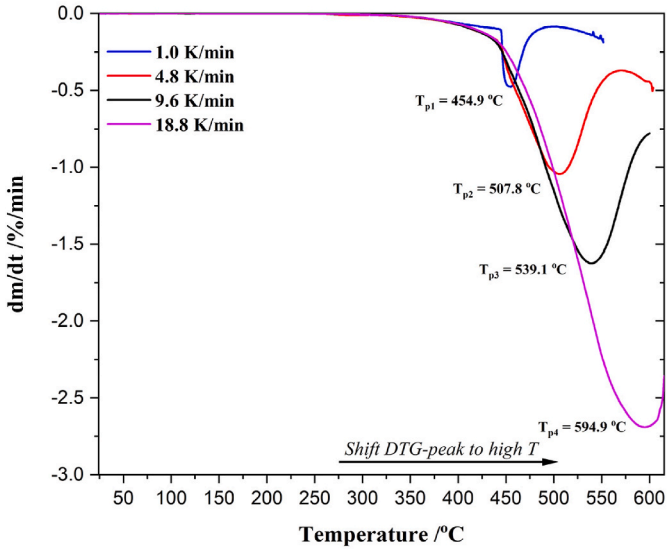


Fig. 2. DTG curves of reduction process of TeO_2 under a hydrogen atmosphere, at the heating rates of β = 1.0, 4.8, 9.6 and 18.8 K/min, respectively. The corresponding T_p (T_{p1} (1.0 K/min), T_{p2} (4.8 K/min), T_{p3} (9.6 K/min) and T_{p4} (18.8 K/min)) values were also designated.

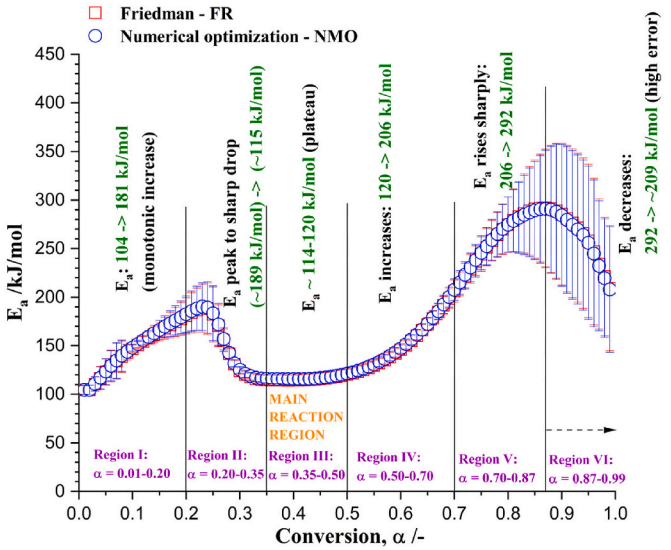


Fig. 3. Conversion-dependent effective activation energy (E_a) values, estimated by applying Friedman (FR) and the numerical optimization (NMO) isoconversional methods, for non-isothermal reduction process of TeO_2 by H_2. Standard deviations (±*Error*) of E_a's are presented as vertical error bars. The corresponding division into mechanistic regions was clearly indicated.

commonly associated with complex mechanisms involving multiple reaction pathways or distributed activation energies. The peak intensity also increases with heating rate (Fig. 2), which is consistent with accelerated reaction kinetics at the elevated temperatures. However, this increase is accompanied by a gradual change in the dominant controlling mechanism. At lower heating rates (~1.0 K/min), sufficient time is available for surface chemical reaction to dominate during early stages of reduction. As the heating rate increases, diffusion of H_2 inward and H_2O outward becomes significant, especially near and beyond the DTG maximum. This indicated a mixed control regime involving both interfacial reaction and product-layer diffusion [42]. Furthermore, the consistent shape of the DTG curves throughout heating rates (Fig. 2), despite their temperature shift, suggests that the underlying reaction mechanism remains unchanged, with heating rate primarily affecting the rate at which the system progresses, through the same sequence of reaction steps.

3.2. *Isoconversional (model-free) kinetic analysis of non-isothermal reduction process of TeO_2 by hydrogen*

Fig. 3 shows the isoconversional dependence of effective (apparent) activation energy (E_a) for non-isothermal reduction of TeO_2 by hydrogen, obtained using the Friedman (FR) and numerical optimization (NMO) methods (section S·II., within Supplementary Material).

From the overall trend of E_a with conversion (Fig. 3), the non-monotonic behavior indicates clear mechanistic transitions during reduction process, ranging from ≈ 104 kJ/mol up to 292 kJ/mol. A high scattered E_a values is behavior occurs at high α values, which is attributed to diffusion effects and increase numerical sensitivity. From Fig. 3, the following mechanistic regions can be observed:

Region I: This region is characterized by monotonic increase in the E_a, suggesting an initially surface-controlled reduction accompanied by the formation of oxygen vacancies. The increasing E_a indicates a progressively higher barrier, which may arise from depletion of reactive surface sites and restructuring of TeO_2 surface during reduction. The continuous increase in the E_a value further suggests a transition from physisorption-dominated behavior to chemisorption-controlled kinetics.

Region II: This region represents the mechanistic transition zone, i.e., the overlap of nucleation processes and the onset of bulk reduction. This is the position where the DTG peak begins to form (see above results). The abrupt decrease in E_a value suggests on the activation of a more energetically favorable bulk reaction pathway (Fig. 3).

Region III: This region corresponds to the *main reaction region*, where the dominant $TeO_2 \rightarrow Te$ reduction occurs, and a stable mechanism is being established. A single controlling step dominates this region, corresponding to the DTG maximum (Fig. 1). The nearly constant E_a values (plateau region) indicate a kinetically uniform regime, governed by interface-controlled reduction.

Region IV: For α > 0.50, there is an increase in the E_a, from ~120 kJ/mol to 206 kJ/mol (α ≈ 0.70), which represents the transition toward diffusion limitations, where the formation of metallic Te layer restricts hydrogen transport and slows the reaction rate.

Region V: In this region, the E_a rises sharply indicating the onset strong diffusion-controlled regime. Here, the metallic Te product layer becomes the dominant factor governing the reaction kinetics.

Region VI: The current region represents the final stage of reduction process. This region is characterized by the presence of the small remaining fraction and presence of numerical instability (Fig. 3). Consequently, larger errors in the calculated E_a values are observed.

Considering the error analysis (ΔE_a (±*Error*)) presented in Fig. 3, it can be concluded the following facts: a) low α → the moderate error, b) medium α (≈0.30 – 0.60) → minimum error, and c) high α → the large error.

The isoconversional kinetic analysis confirms that the reduction of TeO_2 proceeds through a complex multi-step mechanism, for which no single E_a value is sufficient to describe the overall process. The pronounced variation of E_a with conversion (α) indicates the presence of overlapping reaction pathways and suggests distributed activation energy behavior involving surface-controlled, interface-controlled, and diffusion-limited regimes.

Table 1
Correlation of conversion-dependent effective activation energies (E_a) with main properties (regarding process stages) of TG-DTG curves.

TG-stage	α-range	E_a behavior	Mechanism
1	0.01 – 0.05	Low E_a	Desorption
2	0.05 – 0.20	Increasing E_a	Surface reaction
3	0.20 – 0.70	Plateau plus transition	Bulk reduction
4	0.70 - ~0.92	High E_a	Diffusion

Table 1 correlates E_a–α behavior shown in Fig. 3, with the characteristics of provided TG-DTG curves (Fig. 1). At lower conversion degrees, the process is characterized by the surface-controlled reactions and the formation of active sites. Toward transition region and establishing the stable E_a-plateau, the dominant bulk reduction stage takes place. At higher conversions, where E_a increases sharply, it comes to the onset of diffusion limitations, due to the formation of a product layer. Within this analysis, it should be noted that the evolution of the values of the logarithm of effective pre-exponential factor (*logA*) with conversion, obtained by applying both isoconversional methods, is completely identical to that shown in the case of E_a values in Fig. 3, and these results are attached to Fig. S2 in the Supplementary Material.

Fig. 4 shows the linear correlation between the logarithm of pre-exponential factors (*logA*) and apparent activation energies (E_a) obtained from Friedman's (FR) isoconversional method (similar linear correlation plot was derived from NMO method), for non-isothermal reduction of TeO_2 under hydrogen (H_2) atmosphere.

Fig. 4 also shows the mean and predicted confidence ellipses, which visually indicate the strength of the linear relationship between *logA* and E_a values, the uncertainty in the estimated population mean, and the range of a new observation. From the slope (b) and the intercept (a) of the linear equation in a form $logA = a + b{\cdot}E_a$, the isokinetic temperature (T_{iso}) and the isokinetic rate constant (k_{iso}) can be determined, as: $T_{iso} = 1/b{\cdot}R$ (R is the universal gas constant, 8.314 J/(mol·K)), and $a = \log(k_{iso}) \rightarrow k_{iso} = 10^a$. From Fig. 4, it can be observed that both confidence ellipses are narrow and elongated, which indicates the strong correlation between kinetic parameters, where only few pair of data points are located inside the mean confidence ellipse (i.e., this ellipse shows the region where the true population mean for the pair of variables is expected to lie with a certain probability (e.g., 95 %)). Considering the shapes of ellipses, it is clear that there is a high certainty and precision among the kinetic parameters which were derived. Table 2 lists the values of a, b, k_{iso} and T_{iso}, for non-isothermal reduction process of TeO_2 by H_2.

Namely, this linearity indicates that the variations in the E_a are systematically accompanied by corresponding changes in the *logA*, reflecting a thermodynamic coupling between enthalpic and entropic contributions. It can be seen that the obtained value of isokinetic temperature (T_{iso} = 1939.98 K (≈1666.8 °C)) is significantly higher than experimental temperature range, which has the following important implications, as: a) it indicates that the system follows a *true compensation effect*, rather than an artificial correlation arising from data processing, b) the high T_{iso} suggests that enthalpy variations dominate over entropy contributions within the studied temperature interval, and c) the reaction pathways remain mechanistically related throughout the conversion, without abrupt changes in the rate-determining step. Additionally, the isokinetic rate constant amounted $k_{iso} = 0.00879\ s^{-1}$, represents the hypothetical rate at which all reaction steps would proceed identically at T_{iso}. Although this temperature lies far above experimental conditions, the k_{iso} may serves as the useful descriptor of the intrinsic kinetic scale of the investigated system. On the other hand, the intercept $a = -2.056\ s^{-1}$ (Table 2) reflects the baseline entropy contribution to the pre-exponential factor. Considering its relatively small magnitude, this may indicate that the system exhibits moderate entropy variation over the conversion, while dominant compensation arises from changes in activation enthalpy. The existence of a well-defined isokinetic temperature further confirms that the reaction proceeds through a family of related activated complexes, while also supporting the physical significance of the kinetic parameters obtained from the isoconversional (model-free) analysis. Consequently, the high T_{iso} value relative to the experimental range, indicates a true compensation effect and suggests that reduction process proceeds through closely related mechanisms, whereby corresponding isokinetic rate constant reflects an intrinsic kinetic scale, while the compensation behavior (Fig. 4) supports a transition from surface-controlled to diffusion-limited regimes.

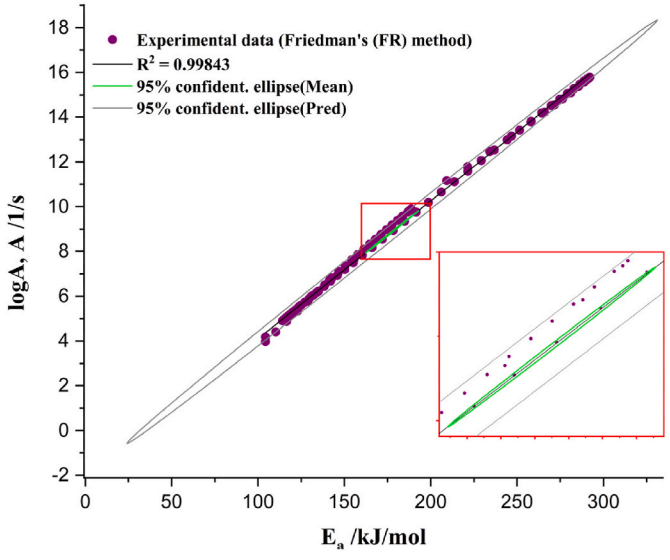


Fig. 4. Linear correlation between *logA* and E_a values (Friedman's (FR) method), for non-isothermal reduction process of TeO_2 by H_2. The coefficient of determination (R^2): $R^2 = 0.99843$.

Table 2
The values of a, b, k_{iso} and T_{iso}, for non-isothermal reduction process of TeO_2 in a hydrogen (H_2) atmosphere.

$logA = a + b{\cdot}E_a$ (the linear relationship)	
a (s^{-1})	−2.056 ± 0.046
b (mol·(kJ)$^{-1}$)	0.062 ± /-
k_{iso} (s^{-1})	0.00879
T_{iso} (K)/[°C]	1939.98 [1666.83]

3.3. Results of DAEM analysis

To account for the multi-step nature of the process, the distributed activation energy model (DAEM) was applied. The activation energy distribution was established, based on the procedure described in section S·III., within Supplementary Material. From results presented in the previous sub-section, the variation of activation energy with conversion, reflects the underlying distribution of activation energies, confirming the suitability of the DAEM approach for describing the investigated reduction process. Additionally, the identified compensation arises from overlapping energetic states and the transition between reaction mechanisms. So, the true physical processes which arise from the isoconversional $E_a(\alpha)$ data (Fig. 3) are the following: a) the surface/initial reduction, b) the main bulk reduction, and c) the diffusion-controlled stage. Fig. 5 a) shows the total, the complex $f(E)$ distribution function (compare section S·III. in Supplementary Material) for non-isothermal reduction of TeO_2 by H_2, which was deconvoluted into a four reaction components, designated as the component I, II, III, and IV, respectively. Consequently, the activation energy distribution, $f(E)$, clearly shows a multi-modal structure, consisting of four component Gaussian functions which represent multiple reaction pathways, and this is in an excellent agreement with isoconversional (model-free) reactions profile (Fig. 3).

Considering the generated total $f(E)$ (Fig. 5 a)), which is fully consistent with isoconversional $E_a(\alpha)$ data, its main features are as follow: a) peak at ~ 120 kJ/mol represents the dominant bulk reduction, b) the intermediate "shoulder" at about ~140 kJ/mol represents transition processes, c) the high-energy tail (≈220 – 300 kJ/mol) is attributed to diffusion-controlled regime process, and d) the low-energy contribution (≈110 kJ/mol) representing the surface reactions. From these results, it is an obvious that total $f(E)$ exhibits a multimodal profile,

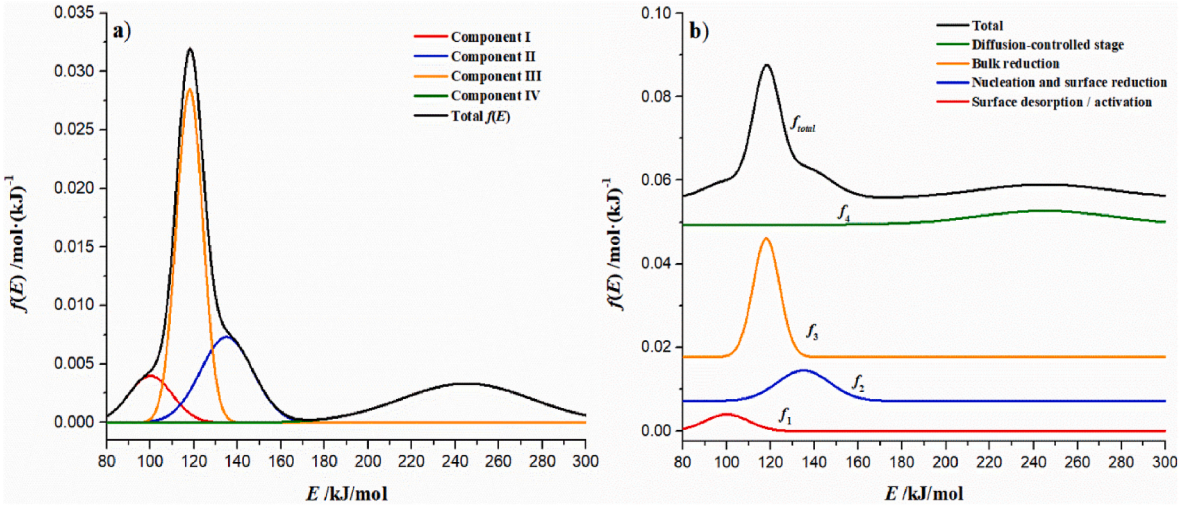


Fig. 5. a) The multi-modal distribution function of activation energies ($f(E)$) (total $f(E)$) approximated by a four component Gaussian functions as Component I, II, III, and IV, respectively. **b)** The view of separate distribution functions (f_1, f_2, f_3, and f_4) together with total $f(E)$ (designated as f_{total}), where f_1, f_2, f_3, and f_4 are attributed to surface desorption and initial activation processes, nucleation and surface reduction phenomena, the main reduction step (bulk reduction – the dominant component), and diffusion-controlled processes, respectively.

reflecting the co-existence of multiple reaction pathways. The dominant peak at ~120 kJ/mol corresponds to the primary reduction of TeO_2 to Te, while the high-energy tail (Fig. 5 a)) is attributed to diffusion limitations at the advanced conversion stages. However, by simplifying this complex activation energy distribution function into its individual distribution components, it can be clearly seen from Fig. 5 b) that each component has its own physical meaning, describing the specific reactions that occur during the reduction process. In this way, they perform mechanistic mapping according to the results shown in Fig. 3. Therefore, Table 3 shows a comparison of the isoconversional results with those obtained *via* the DAEM approach.

It should be noted as an important fact that although partial overlap between low-energy components exists, their separation is justified by the distinct trends observed in the $E_a(\alpha)$ dependence at low conversions. Considering the results presented in Fig. 5b)–Table 4 lists the values of fully deconvoluted four peak DAEM features, including corresponding distribution parameters (Supplementary Material).

It can be seen from Table 4 that component I (Peak 1) is shifted to 100 kJ/mol which is fully separated from the remaining components (Fig. 5 b)). Peak 2, associated with component II, is centered at 135 kJ/mol indicating distinct nucleation, whereas component III with sharpened peak 3 ($\sigma = 6$ kJ/mol) represents the dominant narrow peak (Fig. 5 b)). Finally, the peak 4 (component IV) which is wide, describes a realistic diffusion tail (see Fig. 5 b)). Therefore, the narrow width of dominant peak indicates well-defined kinetic pathway, while broader distributions at low and high E-values reflect the heterogeneity in the surface processes and diffusion limitations. Furthermore, a final consistency check can be established through comparison with the Friedman (FR) isoconversion results (Fig. 3). Namely, $E_a(\alpha)$ plateau matches component III (~118 kJ/mol) near the DTG maximum, the low α behavior matches component I and II (surface activation + pre-DTG peak), the increase in E_a at high α values matches component IV, associated with the post-DTG diffusion regime. In addition, the asymmetry observed in the DTG curves (Fig. 2) is consistent with the extended tail of component IV. Finally, the deconvoluted four-peak DAEM distribution provides a physically consistent and statistically robust description of the reduction process, resolving distinct contributions from surface activation, nucleation, bulk transformation, and diffusion-controlled regimes. The multimodal structure of the DAEM distribution provides a physically meaningful representation of the underlying reaction pathways, and is in excellent agreement with activation energy trends obtained from isoconversional kinetic analysis.

Table 3
Comparison between isoconversional data with results of DAEM analysis, for non-isothermal reduction process of TeO_2 in a hydrogen (H_2) atmosphere.

α-range	E_a behavior (kJ/mol)	DAEM component
0.01 – 0.10	~104 – ≈ 130	Peak 1
0.10 – 0.25	Rising to ~ 180	Peak 2
0.30 – 0.70	~115 – 120	Peak 3
> 0.70	~200 – 292	Peak 4

Table 4
The four component DAEM parameters which describe the key reduction stages of TeO_2 in a hydrogen (H_2) atmosphere.

Component	Assigned process	E_i (kJ/mol)	σ_i (kJ/mol)	w_i[a]	Contribution (%)
I	Surface desorption/activation	100	10	0.10	10
II	Nucleation and surface reduction	135	12	0.22	22
III	Bulk reduction ($TeO_2 \rightarrow Te$)	118	6	0.43	43
IV	Diffusion-controlled stage	245	30	0.25	25

[a] The weight. Normalization: $\sum w_i = 1$.

The DAEM model was applied to simulate TG curves at all investigated heating rates. Therefore, in pursuit of this goal, a final optimization of all parameters was carried out. Table 5 lists the values of optimized DAEM parameters and effective peak parameters at various heating rates.

Based on the optimized DAEM distribution parameters and calculated effective peak parameters (Table 5), the simulated DAEM TG-curves at the different heating rates are shown in Fig. S3 (Supplementary Material). As shown in Fig. S3, the DAEM approach successfully reproduces the experimental trends, including the systematic shift of mass loss profiles toward higher temperatures with heating rate. This behavior is a direct consequence of kinetic constraints imposed by finite heating rates. The simulated TG-curves follow the general tendency of the experimental thermoanalytical curves to shift toward higher T with increasing β, consistent with the DTG shown in Fig. 2. Furthermore, the model effectively captures the broadening of reaction intervals and the

Table 5
The optimized DAEM parameters together with derived effective peak parameters, for non-isothermal reduction process of TeO_2 by H_2.

Component	E_i (kJ/mol)	σ_i (kJ/mol)	ln(A_i)	w_i	β (K/min)	T_p (°C)	Effective, E_a (kJ/mol)	ln(A/β)
I	98 ± 3	9	15.8	0.09	1.0	454.9	115	16.1
II	134 ± 4	13	18.1	0.21	4.8	507.8	125	17.5
III	119 ± 2	6	19.5	0.44	9.6	539.1	140	18.3
IV	242 ± 6	32	24.3	0.26	18.8	594.9	170	19.2

increasing overlap of reaction steps at higher heating rates. However, the geometrical shapes of DAEM TG-curves do not fully coincide with the experimental curves (see Fig. 1), indicating that the DAEM approach alone, cannot realistically describe a comprehensive mechanistic scheme of entire reduction process. In particular, the asymmetric shape of the DTG peaks cannot be adequately reproduced using only the DAEM formalism. Therefore, the implementation of an additional process component, namely the SCM approach, becomes necessary, especially in the reduction region where diffusion dominates. The experimental DTG data (Fig. 2) further demonstrate that the systematic peak shift with increasing β corresponds to a kinetically controlled rather than equilibrium-controlled process, in which the reduction mechanism evolves with temperature. In this context, the DAEM analysis clearly confirms the multi-step nature of the reduction process, while the SCM contribution enables a more realistic description of the diffusion-controlled regime.

Finally, it should be clearly noted and emphasized that although the Distributed Activation Energy Model (DAEM) was originally developed to describe systems involving numerous parallel reactions, such as coal and biomass pyrolysis processes, its application in the present study should not be interpreted as implying multiple independent chemical transformations during TeO_2 reduction. Rather, the distributed activation energies represent the statistical distribution of local kinetic barriers associated with the heterogeneous physicochemical environment within the reacting particles. These variations arise from differences in particle morphology, crystal defects, grain boundaries, the local oxygen-binding environments, the nucleation and growth of metallic tellurium, progressive development of the product layer, and the gradual increase in diffusion resistance, as the reaction proceeds. Consequently, the apparent overlap described by the DAEM reflects the co-existence of partially reduced regions exhibiting different local kinetic characteristics rather than multiple parallel chemical reactions, thereby providing a physically meaningful description of the evolving kinetic heterogeneity during the hydrogen reduction.

3.4. *Shrinking core model and diffusion-controlled regime in the reduction process*

To address the limitations of DAEM approach, the shrinking core model (SCM) was applied to high conversion region. The linearization of diffusion-controlled SCM equation, expressed by Eq. (S9) (Supplementary Material), resulted in an excellent linear fits for α > 0.60,

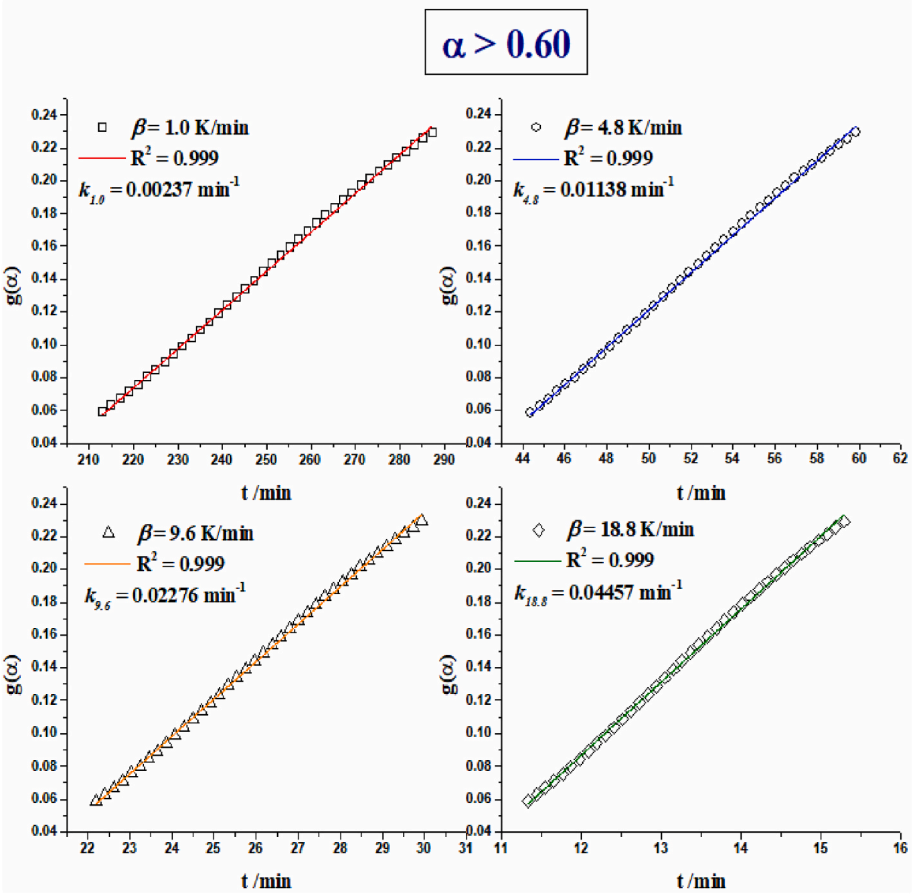


Fig. 6. SCM plots as $g(\alpha) = 1 - (2/3)\cdot\alpha - (1-\alpha)^{2/3}$ *vs.* t (time) at the different heating rates (β = 1.0, 4.8, 9.6 and 18.8 K/min), for α > 0.60 (the values of $k_{1.0}$, $k_{4.8}$, $k_{9.6}$ and $k_{18.8}$ [k_β] represent the values of effective diffusion rate constants, considering each heating rate used). R^2 is the coefficient of determination (=0.999).

confirming that diffusion through the product layer is the rate-limiting step in this region. The corresponding $g(\alpha)$ *vs.* t plots at the different heating rates (1.0, 4.8, 9.6 and 18.8 K/min), where $g(\alpha) = 1 - (2/3)\cdot\alpha - (1-\alpha)^{2/3}$, are shown in Fig. 6.

The rate constants obtained from SCM analysis increases with the heating rate (β), reflecting enhanced reaction kinetics at higher temperatures. Additionally, the Arrhenius plot analysis of these rate constants (Eq. (S10) in Supplementary Material), where the temperature corresponding to $\alpha = 0.70$ were selected for each heating rate, yielded the E_a value of 169.61 kJ/mol. This value corresponds closely to the transition toward diffusion limitations observed in (Fig. 3), as well as to the diffusion-controlled process (f_4 in Fig. 5 b), and the effective E_a value for component IV in Table 5. This result is in good agreement with the onset of diffusion restrictions associated with the formation of the metallic Te.

These findings demonstrate that the reduction process transitions from the chemically controlled kinetics at the low and intermediate conversions to diffusion-controlled behavior at higher conversions [43]. Such transitions are commonly observed in hydrogen reduction systems, and are of particular importance for process optimization in the industrial applications [44–49].

3.5. Results of hybrid DAEM-SCM modeling of non-isothermal reduction of TeO_2 by hydrogen

A hybrid modeling approach combining DAEM and SCM was developed to describe the entire conversion range of reduction process. In this framework, DAEM accounts for the kinetically controlled stages, while SCM captures the diffusion-controlled regime. It should be emphasized that DAEM and SCM describe complementary aspects of the reduction process rather than identical physical phenomena. The DAEM accounts for the intrinsic heterogeneity of reactive sites through a continuous activation energy distribution, whereas the SCM describes the evolution of the reaction front and the increasing influence of product-layer diffusion at the particle scale. Accordingly, the transition between these two descriptions is assumed to occur within a continuous mixed regime, rather than across a sharp interface. The weighting parameter (Supplementary Material) should be understood as an effective phenomenological coupling coefficient, representing the relative contribution of distributed intrinsic kinetics and diffusion-controlled transport to the overall magnitude of reduction rate. To model the experimental kinetic curves, the diffusion parameters of the SCM model were determined according to the procedure described in S·V.2. in Supplementary Material. The estimated diffusion kinetic parameters ($E_{a,d}$, A_d) together with onset temperatures of diffusion control at different heating rates (β), are listed in Table 6.

It can be seen from Table 6, that the diffusion onset temperature, T_d, shifts to higher values with increasing of β. This shift, corresponding to an average conversion of $\alpha \approx 0.85$ across all heating rates, indicates a delayed onset of diffusion control at higher heating conditions. The obtained $E_{a,d}$ values (approx. 240 – 250 kJ/mol) are characteristic of diffusion through a dense metallic product layer [46,50]. On the other hand, the relatively high A_d ($\sim 10^{11}$ s^{-1}) reflects the strong temperature dependence of diffusion process, while the slight increase of $E_{a,d}$ with β can be attributed to thermal shift effects and the kinetic compensation effect (KCE) (see the sub-section 3.2.). These kinetic parameters confirm that the late-stage of considered reduction process is governed by the diffusion through the product layer. Additionally, these quantities should be interpreted as effective Arrhenius parameters derived from the non-isothermal fitting, not purely the intrinsic diffusion coefficients.

Considering all the results presented above, the hybrid DAEM-SCM model (section S·V., Supplementary Material) provides a physically meaningful interpretation of the overall reaction mechanism by linking the kinetic parameters to specific stages of the process. The final kinetic parameters for TeO_2 reduction by H_2 obtained from the hybrid DAEM-SCM modeling, together with their statistical uncertainties (95 % confidence interval), are presented in Table 7. The final values were obtained by an optimization process through nonlinear parameter estimation. A complete description of this procedure, for obtaining the final parameters is described in detail within Supplementary Material. In addition, the statistical uncertainty analysis and the model validation metrics for hybrid DAEM-SCM fitting of non-isothermal reduction process were presented in Table S1 (Supplementary Material).

The hybrid DAEM-SCM model parameters obtained in Table 7 show that the increase of $E_{a,\mathrm{DAEM}}$ with heating rate reflects thermal shift and kinetic complexity of the reduction process, while the high $E_{a,\mathrm{SCM}}$ values confirms diffusion through a dense Te layer. The weighing parameter w ($w \approx 0.70$) indicates that the process is predominantly kinetically controlled, with significant diffusion contribution. In addition, the onset of diffusion limitations is observed above $\alpha \sim 0.60$. The fitted parameter T_p increased systematically with the heating rate, reflecting the thermal shift of the reaction peak under non-isothermal conditions. Similarly, the rate constant (k) increases with heating rate, which is consistent with enhanced mass transport at higher temperatures.

Fig. 7 shows the comparison between experimental $\alpha(T(\mathrm{K}))$ curves at various heating rates and modeled $\alpha(T(\mathrm{K}))$ curves using hybrid DAEM-SCM model, for non-isothermal reduction process of TeO_2 by H_2.

As shown in Fig. 7, excellent agreement is achieved between the experimental conversion curves and the conversion curves generated by applying the hybrid DAEM-SCM model for the non-isothermal reduction of TeO_2 by hydrogen. Statistical evaluation of fitting quality (Table S1; Supplementary Material) further confirms the robustness of the model. The low RMSE (<0.005), the residual mean ≈ 0, small residual standard error, and relative error below 5 %, indicate excellent agreement with the experimental conversion data, absence of systematic bias, stable fitting behavior, and high predictive accuracy. On the other hand, the AIC decreases with increasing β, suggests improved model robustness. Therefore, the hybrid DAEM-SCM model provides a highly accurate and statistically robust description of the non-isothermal reduction of TeO_2 by H_2. The obtained parameters exhibit clear physical trends with the heating rate, while the low residuals and narrow confidence intervals confirm the reliability of the fitted model. Consequently, the combined statistical indicators ($R^2 \geq 0.995$, the low RMSE, and favorable AIC values) (Table S1) demonstrate that the proposed hybrid approach effectively captures both, the kinetically controlled and diffusion-limited regimes of reduction process.

It should be emphasized that the proposed transition from interface-controlled chemical reaction to diffusion-influenced reduction is inferred from the combined kinetic evidence obtained in the present study, rather than from direct experimental observation of the reaction front.

Table 6
The diffusion kinetic parameters and T_d values at the onset of diffusion control, for non-isothermal reduction of TeO_2 by H_2.

β (K/min)	T_d (°C)	$E_{a,d}$ (kJ/mol)	95 % CI[a]	ln(A_d)	A_d (s^{-1})
1.0	522	238.0 ± 5.4	227.4 – 248.6	25.75	$1.52 \times 10^{11} \pm 0.28 \times 10^{11}$
4.8	552	242.1 ± 5.9	230.4 – 253.6	26.11	$2.18 \times 10^{11} \pm 0.34 \times 10^{11}$
9.6	581	246.0 ± 6.3	233.7 – 258.3	26.44	$3.05 \times 10^{11} \pm 0.46 \times 10^{11}$
18.8	610	251.2 ± 6.9	237.5 – 264.5	26.95	$4.62 \times 10^{11} \pm 0.62 \times 10^{11}$
Average	566.3	244.3 ± 6.1	232.3 – 256.3	26.31	$2.84 \times 10^{11} \pm 0.43 \times 10^{11}$

[a] 95 % confidence interval (CI) [kJ/mol], related to statistical uncertainty analysis.

Table 7
The final kinetic parameters with statistical uncertainty (95 % CI) of hybrid DAEM-SCM model, for modeling of non-isothermal reduction process of TeO_2 by H_2.

β (K/min)	$E_{a,DAEM}$ (kJ/mol)	95 % CI[a]	ln(A), A (s^{-1})	$E_{a,SCM}$ (kJ/mol)	k (s^{-1})	Diffusion regime (α)	T_p (°C)	T_d (°C)	w[b] (–)	R^2
1.0	115.0 ± 2.6	109.9 – 120.1	18.2 ± 0.42	238.0 ± 5.4	0.0095 ± 0.0006	$\alpha > 0.60$	482.0 ± 3.1	522.0 ± 3.8	0.71 ± 0.018	0.995
4.8	128.0 ± 3.1	121.9 – 134.1	19.5 ± 0.47	242.1 ± 5.9	0.0118 ± 0.0007	$\alpha > 0.62$	512.0 ± 3.5	552.0 ± 4.2	0.70 ± 0.017	0.996
9.6	142.0 ± 3.6	134.9 – 149.1	20.8 ± 0.53	246.0 ± 6.3	0.0139 ± 0.0008	$\alpha > 0.63$	541.0 ± 3.9	581.0 ± 4.6	0.69 ± 0.016	0.997
18.8	158.0 ± 4.2	149.8 – 166.2	22.3 ± 0.61	251.2 ± 6.9	0.0162 ± 0.0010	$\alpha > 0.65$	592.0 ± 4.5	610.0 ± 5.3	0.68 ± 0.015	0.998

[a] 95 % confidence interval (CI) [kJ/mol], related to statistical uncertainty analysis.
[b] The contribution of DAEM (the kinetic control fraction); the weighting parameter (w - fractional contribution) should not be interpreted as a geometric quantity, interface thickness, or directly measurable physical property. This parameter was introduced as an effective phenomenological coupling coefficient that quantifies the relative contribution of the distributed intrinsic kinetics represented by the DAEM and the diffusion-controlled behavior represented by the SCM, in reproducing the experimentally observed reduction rate (see also Supplementary Material, within section S·V.). Thus, w reflects the evolving balance between these two simultaneously operating kinetic contributions during the overall reduction process.

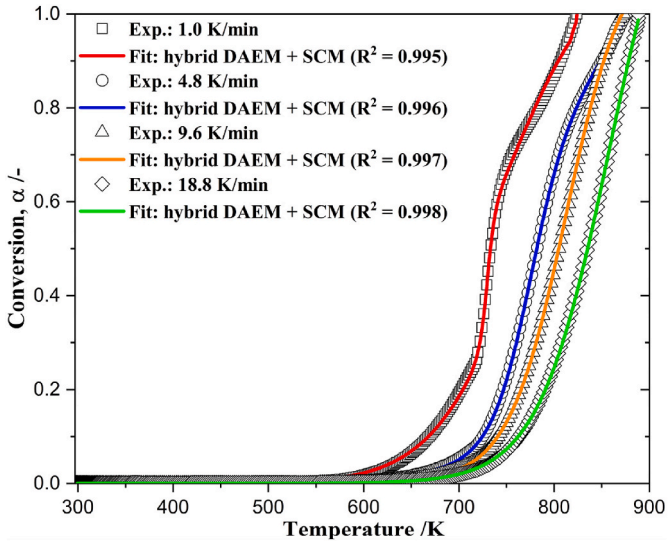


Fig. 7. Experimental and fitted hybrid DAEM-SCM model conversion (α) – temperature (K) curves at the heating rates of 1.0, 4.8, 9.6 and 18.8 K/min, for non-isothermal reduction process of TeO_2 in a hydrogen (H_2) atmosphere.

This interpretation is supported by the systematic evolution of the apparent activation energy with conversion, the excellent agreement between the experimental conversion - T data and the integrated DAEM-SCM model (Fig. 7), and consistency of the optimized mechanistic functions over the investigated temperature range. Nevertheless, the present results do not constitute independent experimental proof of the product-layer diffusion. Direct verification of the progressive development of diffusion resistance would require the complementary microstructural characterization techniques, such as cross-sectional SEM/EDS analysis, *in situ* high-temperature microscopy, or X-ray computed tomography of the partially reduced particles. Such investigations would provide valuable insight into the evolution of the reaction front and represent an important direction for the future studies.

Since that all thermo-analytical measurements were performed under identical and carefully controlled experimental conditions using a constant sample mass and hydrogen flow rate, they have clearly ensured excellent reproducibility throughout the experimental program. Although minor heat- and mass-transfer effects associated with the powder bed cannot be entirely excluded, particularly at higher conversions, the systematic consistency of the TG-DTG profiles obtained at different heating rates and their excellent agreement with the optimized kinetic models, indicate that these effects did not adversely affect the precision of the kinetic calculations, or the overall mechanistic interpretation presented in this research.

Table 8 provides the comparison of kinetic parameters for hydrogen reduction systems, including the model proposed in this study with literature data.

The results presented in Table 8 show that the DAEM E_a (115 – 158 kJ/mol) are comparable to those reported for Fe-oxide reduction (80 – 200 kJ/mol), confirming the characteristic kinetics of hydrogen reduction processes. In contrast, the SCM E_a (~240 – 250 kJ/mol) matches the diffusion-controlled regimes in the NiO reduction and the coke gasification. The mechanistic interpretation obtained in this study is also consistent with literature observations, where the early stage of the reduction are governed primarily by chemical reaction control, while the later stages become diffusion controlled. In the present model, this transition occurs at approximately α ~0.6, separating the kinetically controlled DAEM regime from the diffusion-controlled SCM. An important novelty of this work is the integration of DAEM, SCE, and ECC (see results in later section) approaches within a unified kinetic framework. Most literature studies employ either isoconversional methods, multi-step kinetic models, or SCM analysis independently, whereas combined DAEM-SCM-EEC modeling has rarely been reported for hydrogen reduction systems. The consistency of the obtained activation energies with literature values for Fe_2O_3, Fe_3O_4, and NiO further supports the physical validity of the proposed model.

3.6. Thermodynamic analysis of reduction process

Based on the computation procedure described in section S·VI. of Supplementary Material, the values of activation enthalpy ($\Delta H^{\#}$), entropy ($\Delta S^{\#}$), and Gibb's free energy ($\Delta G^{\#}$) were estimated. Fig. 8 a) – c) shows the variation of thermodynamic activation parameters ($\Delta H^{\#}$, $\Delta S^{\#}$ and $\Delta G^{\#}$) with conversion (α), which can provide an important insight into the evolving mechanism of TeO_2 reduction process by hydrogen.

As shown in Fig. 8 a), the activation enthalpy ($\Delta H^{\#}$) initially increases from ~100 kJ/mol at lower conversion ($\alpha < 0.20$) to ~ 180 kJ/mol, indicating that the early stage of reduction process is governed by surface chemical reactions requiring progressively higher energy barriers. This increase reflects the consumption of more reactive surface sites and the transition toward less reactive bulk material. In the intermediate conversion region ($\alpha \approx 0.25 – 0.50$), $\Delta H^{\#}$ decreases to ~ 110 kJ/mol, suggesting on temporary facilitation of the reaction, possibly due to the structural re-arrangement, defect generation, or the enhanced gas accessibility. At higher conversions (for $\alpha > 0.60$), $\Delta H^{\#}$ increases sharply, reaching ≈ 280 kJ/mol, which is characteristic for the diffusion-controlled processes through a dense product layer. This behavior is consistent with the formation of metallic Te, which imposes the significant mass transfer resistance [58].

The activation entropy (Fig. 8 b)) exhibits strongly negative values at

Table 8
Comparative overview of kinetic parameters for hydrogen reduction systems (DEAEM-SCM vs literature data).

Reaction system	Method	E_a (kJ/mol)	ln(*A*)	Model type	Diffusion regime	Temperature range (°C)	Key mechanism	Reference
TeO_2 (this study)	DAEM	115 - 158	18.2 - 22.3	Distributed kinetics	Not explicit	~350 - 620	Multi-step surface + bulk reduction	This study
TeO_2 (this study)	SCM	238 - 251.2	-	Diffusion-controlled	$\alpha > 0.60$	~500 - 620	Product layer diffusion	This study
TeO_2 (this study)	DAEM-SCM	115 – 251.2	18 - 22	Hybrid (DAEM + SCM)	$\alpha > 0.60$	RT – 620	Kinetic → diffusion transition	This study
Fe_2O_3	Multi-step TGA deconvolution	~80 - 160 (stage-dependent)	-	Multi-step kinetic model	Yes	750 - 950	Nucleation + growth	[51]
Fe_3O_4 (magnetite)	Multi-step modeling	Wide range (step-dependent)	-	Parallel/series model	Yes	600 - 900	Multi-stage reduction	[52]
Hematite (Fe_2O_3)	Isoconversional (FWO/Starink)	79 - 86	-	Model-free	Yes	500 - 800	Multi-stage reduction	[53]
Fe-oxide pellets	Multi-step; Arrhenius	90 – 200 (+)	-	Multi-reaction kinetic	Yes	600 - 1000	Coupled reactions	[54]
NiO	SCM-based kinetics	150 - 250	-	Shrinking core model	Strong	500 - 1000	Product layer diffusion	[55]
Cu_2O	TGA kinetics	80 - 140	-	Reaction-controlled	Limited	200 - 500	Surface reaction	[56]
Coke gasification (DAEM)	DAEM	200 - 290	-	Distributed activation energy model	Yes	700 - 1000	Surface + pore diffusion	[57]

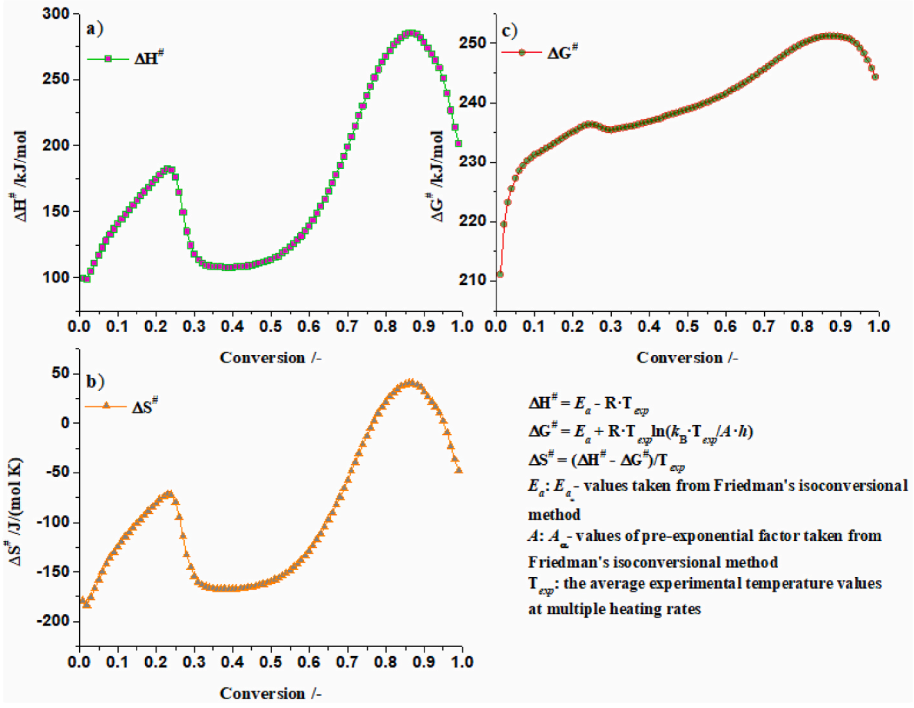


Fig. 8. The variation of thermodynamic activation parameters with conversion: **a)** activation enthalpy ($\Delta H^{\#}$), **b)** activation entropy ($\Delta S^{\#}$), and **c)** Gibb's free energy of activation ($\Delta G^{\#}$), for non-isothermal reduction process of TeO_2 by H_2.

low conversion (−180 J/(mol·K) to −80 J/(mol·K)), indicating the formation of highly ordered transition states during the initial surface reaction. Such negative $\Delta S^{\#}$ values are typical for adsorption-controlled processes, where the reactant molecules lose degrees of freedom upon interaction with the solid surface [34]. With increasing the conversion, $\Delta S^{\#}$ becomes less negative and eventually positive ($\alpha \approx 0.70$ - 0.90), reaching the values up to ≈ + 40 J/(mol·K). This transition reflects an increase in disorder in the activated complex, which can be attributed to the development of the porous or defective structures, and the onset of the diffusion pathways within the product layer. The observed trend is consistent with a shift from the surface-controlled to diffusion-controlled mechanisms [59].

The Gibbs free energy of activation (Fig. 8 c)) shows a relatively smooth and monotonic increase from ~210 kJ/mol to ~250 kJ/mol over the entire conversion range. Unlike $\Delta H^{\#}$ and $\Delta S^{\#}$, the $\Delta G^{\#}$ does not exhibit strong fluctuations, indicating that the overall energetic barrier of the process remains relatively stable, despite the significant variations in the enthalpic and entropic contributions. Namely, this behavior is a hallmark of the enthalpy-entropy compensation (EEC) effect, where increases in $\Delta H^{\#}$ are the offset by corresponding increases in $\Delta S^{\#}$, resulting in a nearly constant $\Delta G^{\#}$. Possible presence of EEC can suggest that reaction proceeds *via* the family of the closely related mechanisms, with the similar free energy barriers but differing energetic and configurational characteristics [42].

Combined trends of $\Delta H^{\#}$, $\Delta S^{\#}$, and $\Delta G^{\#}$ clearly indicate a multi-stage reduction mechanism, where the following cases exist: a)

α < 0.30 - the surface chemical reaction control (the low $\Delta H^{\#}$, negative $\Delta S^{\#}$), b) 0.30 < α < 0.60 - the transition regime with structural evolution, and c) α > 0.60 – the diffusion-controlled regime (the high $\Delta H^{\#}$, positive $\Delta S^{\#}$). Thus, the relatively constant $\Delta G^{\#}$ through the conversion (α) confirms that these stages are thermodynamically coupled *via* the compensation effect, supporting the applicability of the hybrid kinetic models (e.g., DAEM-SCM (see sub-section 3.5.)) for describing the reduction process.

Fig. 9 shows enthalpy-entropy compensation (EEC) plot obtained for non-isothermal reduction of TeO_2 by H_2. The figure also shows confidence ellipses (mean and predicted), together with R^2–value (Eq. (S23) in Supplementary Material).

It can be seen from Fig. 9 that the confidence ellipses in the $\Delta H^{\#}-\Delta S^{\#}$ plot are very elongated and narrow, indicating a strong statistically significant correlation between activation enthalpy and entropy. The narrowness of ellipses further suggests high precision and low uncertainty in determined individual $\Delta H^{\#}$ and $\Delta S^{\#}$ values despite their strong mutual correlation. The thermodynamic compensation analysis for non-isothermal reduction of TeO_2 by hydrogen reveals a well-defined enthalpy-entropy compensation (EEC) behavior, characterized by a compensation temperature of $T_{comp} = 847.16$ K, and the corresponding free energy of compensation of $\Delta G^{\#}_{comp} = 248.36$ kJ/mol (Fig. 9). The relatively constant value of $\Delta G^{\#}_{comp}$ indicates that the overall free energy barrier remains nearly invariant despite significant variations in $\Delta H^{\#}$ and $\Delta S^{\#}$, which is characteristic of compensation phenomena (see above). The obtained T_{comp} lies within the experimental temperature range of reduction process, suggesting that both enthalpic and entropic contributions significantly influence the reaction kinetics. This value represents the temperature at which all reaction steps would exhibit identical rate constants, indicating that the system evolves through a series of closely related activated complexes, rather than distinct mechanistic regimes [60,61].

To distinguish between true (physical) and artificial (statistical) compensation effects, Krug's statistical criterion was applied (sub-section S·VI.1. in Supplementary Material). Table S2 (Supplementary Material) shows the results of Krug's test. The harmonic mean temperature ($T_{hm} = 779.13$ K) is significantly lower than the compensation temperature ($T_{comp} = 847.16$ K), and lies outside the confidence interval: $[T_{comp} - t{\cdot}\sigma, T_{comp} + t{\cdot}\sigma] = [840.41, 853.91]$ K. Since $T_{hm} \notin [T_{comp} \pm t{\cdot}\sigma]$, the null hypothesis of the purely statistical compensation can be rejected. This confirms that the observed EEC behavior has a physical origin,

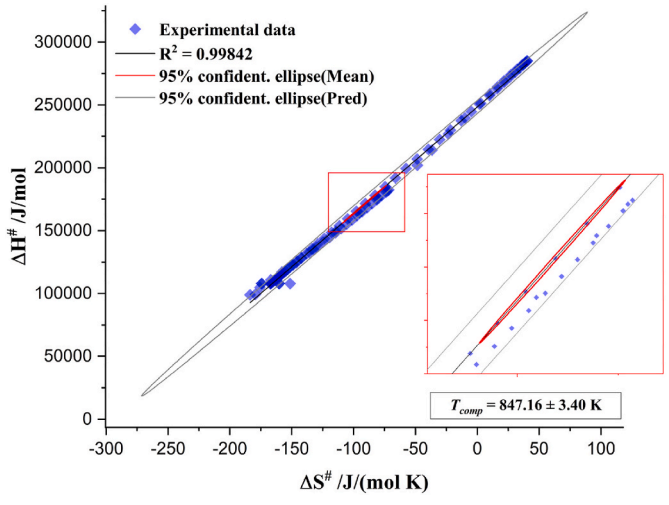


Fig. 9. The enthalpy-entropy ($\Delta H^{\#}-\Delta S^{\#}$) relationship obtained for non-isothermal reduction of TeO_2 by H_2. The compensation temperature obtained from the slope of the $\Delta H^{\#}-\Delta S^{\#}$ plot is: $T_{comp} = 847.16$ K, while the free energy of compensation derived from the intercept is $\Delta G^{\#}_{comp} = 248.36 \pm 0.394$ kJ/mol). The coefficient of determination $R^2 = 0.99842$.

reflecting genuine thermodynamic coupling between $\Delta H^{\#}$ and $\Delta S^{\#}$, rather than an artifact of correlated errors [62]. The presence of a physically justified EEC effect supports the interpretation of the reduction process as a continuous mechanistic evolution. Namely, at lower temperatures and conversions, the reaction is governed by surface chemical processes with lower enthalpy and more negative entropy (ordered transition states). At higher temperatures and conversions, the formation of metallic Te product layer introduces diffusion limitations associated with higher enthalpy and more positive entropy, reflecting increased disorder and defect-mediated transport. The compensation behavior indicates that these mechanistic changes remain thermodynamically coordinated, resulting in a relatively stable free energy barrier throughout the reaction. This finding is also fully consistent with hybrid DAEM-SCM modeling approach, which describes both kinetically and diffusion-controlled regimes (see above).

It should be emphasized that a linear correlation between the Arrhenius parameters does not, by itself, constitute sufficient evidence for a genuine enthalpy–entropy compensation effect, since such relationships may arise from *statistical covariance*, during the parameter estimation or from the experimental uncertainty. For this reason, *the physical significance* of the observed compensation behavior was assessed using *Krug's statistical criterion, rather than relying solely on the Arrhenius compensation relationship*. Agreement of the experimentally determined compensation temperature with the requirements of Krug's test supports the interpretation that the observed compensation effect reflects a genuine thermodynamic phenomenon associated with changes in the reaction mechanism, rather than the purely mathematical artifact, arising from the correlated kinetic parameters.

Furthermore, it is necessary to evaluate whether, in addition to EEC, an isoequilibrium relationship exists. This was examined through the evaluation of *CQF* and the corresponding threshold γ values (sub-section S·VI.1. in Supplementary Material). Fig. S4 (Supplementary Material) shows dependence of the natural logarithm of equilibrium pressure (marked with ln*P*) as a function of the inverse temperature, for non-isothermal reduction process of TeO_2 by H_2. It should be noted that the equilibrium partial pressure ratio used in the Van't Hoff analysis was not measured directly during the non-isothermal thermo-analytical experiments. Instead, for each characteristic experimental temperature, the equilibrium value of the P_{H_2O}/P_{H_2} was calculated from the thermodynamic equilibrium of the reaction: $TeO_{2(s)} + 2H_{2(g)} \rightleftharpoons Te_{(s)} + 2H_2O_{(g)}$. Assuming the unit activities for the condensed phases, the equilibrium constant was related to the standard Gibbs free energy through the relation: $K_p = exp\left(-\frac{\Delta G^o}{RT}\right)$, yielding $ln\left(\frac{P_{H_2O}}{P_{H_2}}\right) = -\frac{\Delta G^o(T)}{(2RT)}$. So, the Van't Hoff plot represents thermodynamically calculated equilibrium partial pressure ratios evaluated at experimentally determined temperatures, rather than directly measured gas-phase pressures. So, considering the theoretical background presented in Supplementary Material (the subsection S·VI.1.), the Van't Hoff plot was constructed using thermodynamically calculated equilibrium partial pressure ratios evaluated at characteristic temperatures, obtained from TG reduction experiments.

The (ln*P*) *vs.* $1/T$ dependence exhibits a nonlinear, sigmoidal-like trend rather than the linear trend from an ideal Van't Hoff relationship. This deviation indicates temperature-dependent changes in the apparent reaction enthalpy and entropy, consistent with the presence of EEC and the evolving nature of the reduction mechanism. The corresponding values of T_{low} and T_{high} define the experimental temperature window and corresponding bounds in $1/T$ space (Fig. S4) ($T^* = 769.23$ K corresponds to the characteristic point where the curvature changes, often associated with the onset of accelerated reduction and structural transformation). The obtained condition, $|(1/T_{\min} - 1/T_{high})| < |(1/T_{min} - 1/T_{low})|$, shown in Fig. S4, implies that $T_{\min}$ is thermodynamically closer to T_{high}, suggesting that the dominant energetic state is shifted toward higher temperature regimes, where diffusion and product-layer effects become significant. Consequently, the reduction process cannot be described by a single equilibrium relationship, but rather by multiple

overlapping conributions involving chemical reaction, diffusion, and phase evolution. This behavior is fully consistent with the distributed kinetic nature predicted by the DAEM framework. From the derived ln*P*-1/*T* plot (Fig. S4), the apparent reaction enthalpy (ΔH_{app}) can be estimated directly from the local slope of the Van't Hoff-type dependence, in a form:

$$lnP = -\frac{\Delta H_{app}}{R} \cdot \frac{1}{T} + const., \quad (4)$$

so

$$\Delta H_{app} = -R\left(\frac{d(lnP)}{d\left(\frac{1}{T}\right)}\right). \quad (5)$$

For each temperature region, i.e., the low temperature region (high $1/T \approx 0.00160$ - $0.00148\ K^{-1}$), the medium temperature region ($1/T \approx 0.00140$ - $0.00130\ K^{-1}$) and high temperature region (low $1/T \approx 0.00122$ - $0.00114\ K^{-1}$) (Fig. S4), two representative points were taken. So, based on Eqs. (4) and (5), the values of ΔH_{app} are calculated. Table 9 lists the values of ΔH_{app} across indicated temperature ranges, including also and their interpretation.

The strong nonlinearity of the ln*P*-1/*T* is reflected in the significant variation of the apparent enthalpy from −64.0 kJ/mol to −300 kJ/mol across the investigated temperature range (Table 9). At higher temperatures (low 1/*T*), the large magnitude of ΔH_{app} suggests an increasing contribution of diffusion-controlled processes, associated with the formation of the metallic Te product layer. In contrast, the smaller enthalpy values observed at lower temperatures are characteristic of surface reaction control with weaker temperature sensitivity. The intermediate region represents a transition regime, where both reaction and transport processes contribute. The progressive increase in $|\Delta H_{app}|$ with temperature is fully consistent with the previously identified EEC effect, supporting the evidence that the system evolves through multiple thermodynamically distinct states, corresponding to changes in the reaction mechanism and mass transport limitations.

The compensation quality factor (*CQF)* provides a quantitative measure of both the degree of coalescence of the Van't Hoff plots and probability of the statistical origin of EEC effect. Using Eqs. (S27) and (S28) (Supplementary Material), the values $CQF = 0.640$ and $K = 2.623$ were obtained. The *K*-factor, which approximatelly represents the ratio $K \approx T_{iso}/T_{hm}$, significantly deviates from the unity, where $K \gg 1$ implies that the T_{iso} is much higher than the harmonic mean temperature (T_{hm}) (Table S2). This indicates that the true isokinetic temperature lies outside the experimental temperature range. Consequently, no strict isokinetic relationship exists, and the system exhibits only a quasi-compensation effect.

Using Eqs. (S29) and (S30) (Supplementary Material), the threshold *CQF* values γ [*N*; CL %] for 95 % and γ [*N*; CL %] for 99 % confidence levels were estimated, and these results are shown in Fig. 10 a) – b), respectively.

Based on the results presented in Fig. 10 a) – b), the obtained value of *CQF* falls outside the colored full-line regions corresponding to both 95 % and 99 % confidence levels. Accordingly, the condition condition $0.9 > CQF \geq \gamma$ [*N*; 99 %] is satisfied (*case b;* – see Supplementary Material), indicating that the observed compensation effect is physically meaningful but does not fulfill the criteria for a strict isokinetic relationship. Combined with the nonlinear Van't Hoff behavior, the moderate *CQF* (=0.640) and high *K*-factor (=2.623), these results suggest that the reduction process proceeds through multiple thermodynamically related pathways rather than through a single globally compensated mechanism. This interpretation is fully consistent with the hybrid DAEM-SCM framework, in which distributed activation energies and diffusion limitations jointly govern the reduction process.

Table 9
Summary of the apparent enthalpies, obtained from the ln*P*–1/*T* dependence (Fig. S4).

Region	1/*T* range (K^{-1})	ΔH_{app} (kJ/mol)	Interpretation
Low *T*	0.00160 – 0.00148	−64.0	Surface reaction/the weak temperature dependence
Middle *T*	0.00140 – 0.00130	−150.0	Transition regime
High *T*	0.00122 – 0.00114	−300.0	Diffusion/the product-layer controlled

The overall thermodynamic and kinetic analysis confirms that the reduction of TeO_2 by H_2 proceeds through a complex multi-step mechanism involving distributed activation energies and a gradual transition toward diffusion-controlled behavior at high conversions. The nonlinear Van't Hoff behavior together with the SCM, EEC, and CQF analyses consistently supports the presence of evolving reaction pathways and thermodynamically coupled kinetic regime.

As a key finding of this study, it should be noted that identification of diffusion-controlled limitations at high conversion highlights the need to optimize particle size, the porosity, and gas flow conditions to enhance the mass transport. Furthermore, the strong dependence of the reaction kinetics on the heating rate suggests that the thermal management plays the critical role in the process efficiency. Combined DAEM and SCM approaches provide a robust framework for predicting the reaction behavior under different operating conditions, which is essential for the design and optimization of hydrogen-driven systems. Therefore, findings present in this research contribute to a deeper understanding of the gas-solid reduction mechanisms, and support development of the efficient and sustainable hydrogen-based technologies.

However, the applicability is subject to several limitations. First, the accuracy of the framework depends on the reliability of the kinetic parameters obtained from the experimental data. The variations in raw material characteristics such as particle size distribution, porosity, and impurity content, may influence the reduction pathway and consequently affect the model predictions. Additionally, the current framework mainly focuses on the intrinsic reaction kinetics under the investigated experimental conditions and does not explicitly account for complex transport phenomena, such as heat transfer limitations or diffusions through porous structures. For larger-scale applications, these factors may become increasingly significant. To extend the applicability of this framework, it is essential to integrate multiscale transport phenomena, validating its applicability across different reduction systems and establishing a more comprehensive predictive model that can be suitable for future reactor-scale processes.

4. Conclusions

The non-isothermal reduction of TeO_2 by hydrogen (H_2) was systematically analyzed using combined kinetic and thermodynamic approaches. To the authors' knowledge, this work provides the first comprehensive kinetic and thermodynamic investigation of the non-isothermal hydrogen reduction of TeO_2. Thermogravimetric measurements revealed a strong dependence of reaction behavior on the heating rate, with the DTG peak shifts and broadening confirming the complex, multi-step nature of the process. The integrated DAEM-SCM (hybrid) model successfully described experimental data, capturing both distributed activation energies and diffusion-related limitations. The apparent activation energy and activation enthalpy varied significantly with the conversion and temperature, increasing from low values characteristic for the surface-controlled reactions to high values (~300 kJ/mol) associated with diffusion through the product layer. This evolution confirms a transition from chemical reaction control to mixed and diffusion-limited regimes.

The ln*P*-1/*T* analysis revealed pronounced nonlinearity, indicating deviation from ideal Van't Hoff behavior and supporting the presence of enthalpy-entropy compensation (EEC). It was confirmed that the

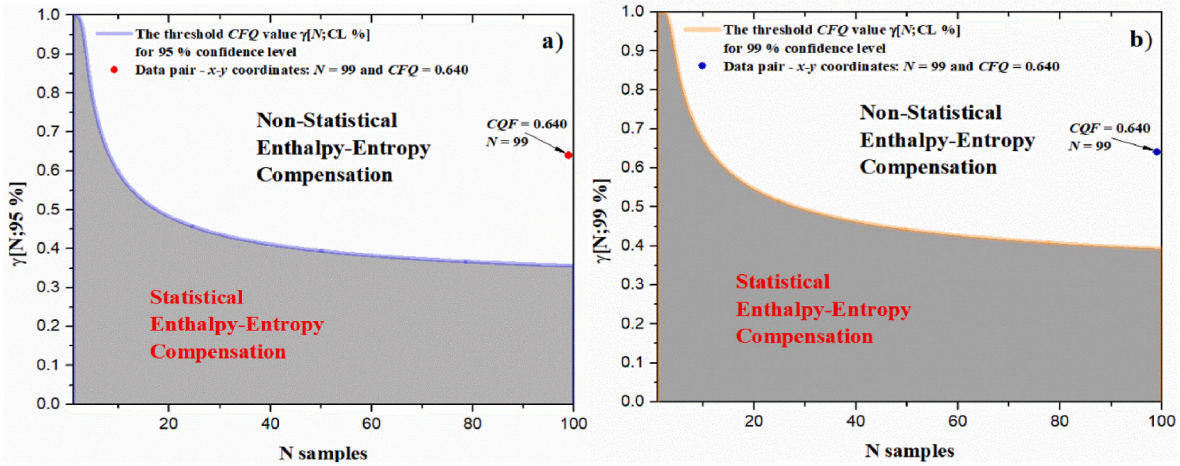


Fig. 10. Threshold *CQF* values γ [*N*; CL %] for: **a)** 95 % (*light blue full line*) confidence level, and **b)** 99 % (*orange full line*) confidence level, described by algebraic expressions given in Supplementary Material, for non-isothermal reduction of TeO_2 by H_2. (For interpretation of the references to color in this figure legend, the reader is referred to the Web version of this article.)

compensation effect is physically meaningful, but does not satisfy the strict isokinetic criteria.

It was concluded that the reduction mechanism is governed by coupled interfacial reaction and gas diffusion (H_2/H_2O), evolving with temperature and conversion. The combined DAEM-SCM-EEC framework provides the robust and physically consistent description of hydrogen-driven TeO_2 reduction, offering valuable insights for the process optimization and reactor design. The integrated kinetic-thermodynamic methodology developed in this study extends beyond the specific TeO_2-H_2 system and establishes a general framework for quantitatively describing complex gas-solid reduction processes, governed by simultaneous intrinsic reaction kinetics and diffusion phenomena. From an engineering perspective, the results demonstrate that possible optimization of particle size, particle morphology, and operating temperature, can effectively reduce internal diffusion limitations, may improve the hydrogen accessibility, and enhance the overall reduction efficiency. These findings provide valuable guidance for reactor design, process intensification, and optimization of hydrogen consumption in industrial reduction technologies. On the other hand, the proposed DAEM-SCM-EEC framework offers a versatile platform for future investigations of hydrogen-based reduction of other metal oxides and complex oxide systems, thereby contributing to the advancement of sustainable hydrogen metallurgy, and supporting the transition toward low carbon metallurgical processing. Therefore, the future work should validate the proposed framework under isothermal conditions, extend it to the industrial reactor scales, and couple the kinetic model with reactor-scale transport simulations to support the design of the sustainable hydrogen-based tellurium production processes.

Data availability

Data will be made available on request.

Declaration of generative AI and AI-assisted technologies in the manuscript preparation process

During the preparation of this work, the author(s) used ChatGPT-5.3 for grammar and language improvement purposes. The author(s) reviewed and edited the output as needed and take full responsibility for the content of the published article.

Funding

This research study was funded by the Federal Ministry for Economic Affairs and Climate Action of Germany (Bundesministerium für Wirtschaft und Klimaschutz), Grant number 03 EN2056C.

CRediT authorship contribution statement

Hanwen Chung: Conceptualization, Data curation, Formal analysis, Investigation, Methodology, Software, Validation, Visualization, Writing – original draft, Writing – review & editing. **Bojan Janković:** Conceptualization, Data curation, Formal analysis, Methodology, Software, Supervision, Validation, Visualization, Writing – original draft, Writing – review & editing. **Semiramis Friedrich:** Project administration, Resources, Supervision. **Bernd Friedrich:** Funding acquisition, Resources, Supervision.

Declaration of competing interest

The authors declare that they have no known competing financial interests or personal relationships that could have appeared to influence the work reported in this paper.

Acknowledgements

Authors would like to acknowledge financial support by the Federal Ministry for Economic Affairs and Climate Action of Germany (Bundesministerium für Wirtschaft und Klimaschutz), grant number 03 EN2056C, and Ministry of Science, Technological Development and Innovation of the Republic of Serbia, under Contract number 451-03-33/2026-03/200017.

Appendix A. Supplementary data

Supplementary data to this article can be found online at https://doi.org/10.1016/j.ijhydene.2026.156980.

References

[1] Brandner U, Antrekowitsch J, Leuchtenmueller M. A review on the fundamentals of hydrogen-based reduction and recycling concepts for electric arc furnace dust extended by a novel conceptualization. Int J Hydrogen Energy 2021;46:31894–902. https://doi.org/10.1016/j.ijhydene.2021.07.062.

[2] Ni M, Leung DYC, Leung MKH, Sumathy K. An overview of hydrogen production from biomass. Fuel Process Technol 2006;87:461–72. https://doi.org/10.1016/j.fuproc.2005.11.003.

[3] Wen ZCH, Teoh YH, How HG, Yaqoob H, Idroas MY, Le TD, Jamil MA, Jamil MM, Shahzad MW. Hydrogen production: current state and future trajectories of development. Energy Convers Manag X 2026;30:101691. https://doi.org/10.1016/j.ecmx.2026.101691.

[4] Turner JA. Sustainable hydrogen production. Science 2004;305(5686):972–4. https://doi.org/10.1126/science.1103197.

[5] Devabharathi N, Yadav S, Dönges I, Trouillet V, Schneider JJ. α-TeO_2 oxide as transparent *p*-type semiconductor for low temperature processed thin film transistor devices. Adv Mater Interfac 2024;11:2301082. https://doi.org/10.1002/admi.202301082.

[6] Poria K, Parmar R, Kumari H, Dhankhar S, Kundu RS. Physical and optical properties of tellurium dioxide-based quaternary glasses: potential for nonlinear optical applications. J Electron Mater 2025;54:172–9. https://doi.org/10.1007/s11664-024-11566-z.

[7] Schlesinger M, Paunovic M. Modern electroplating. fifth ed. Hoboken, New Jersey, USA: John Wiley & Sons, Inc.; 2010. p. 1–701.

[8] Triboulet R, Siffert P. CdTe and related compounds; physics, defects, Hetero- and nano-structures, crystal growth, surfaces and applications - part I: physics, CdTe-based nanostructures, CdTe-based semimagnetic semiconductors, defects. Amsterdam, Netherlands: Elsevier Science; 2010. p. 133–68. https://doi.org/10.1016/C2009-0-17817-0. ISBN: 978-0-08-046409-1.

[9] Chung H, Friedrich S, Qu M, Friedrich B. Hydrogen reduction of tellurium oxide in a rotary kiln, initial approaches for a sustainable process. Crystals 2025;15:478. https://doi.org/10.3390/cryst15050478.

[10] Chung H, Sin YH, Eickhoff M, Friedrich S, Friedrich B. Design and experimental validation of a gas-flow-optimised reactor for the hydrogen reduction of tellurium oxide. Processes 2026;14:33. https://doi.org/10.3390/pr14010033.

[11] Ranjbar A, Aghamiri SF, Irankhah A. Effect of MgO/Al_2O_3 ratio in the support of mesoporous $Ni/MgO\text{-}Al_2O_3$ catalysts for CO_2 utilization via reverse water gas shift reaction. Int J Hydrogen Energy 2023;48:19115–25. https://doi.org/10.1016/j.ijhydene.2023.01.102.

[12] Wang M, Wang Y, Xie W, Wang G, Li T. ZIF-67-derived nickel–cobalt phosphide nanocubes/N-doped carbon/nickel form composite for efficient overall water splitting. Int J Hydrogen Energy 2023;48:19995–20005. https://doi.org/10.1016/j.ijhydene.2023.02.021.

[13] Guo Z, Tian C, Gong K, Xu W, Chen L, Tao W-Q. Experimental study on the dynamic response of voltage and temperature of an open-cathode air-cooled proton exchange membrane fuel cell. Int J Hydrogen Energy 2024;57:601–15. https://doi.org/10.1016/j.ijhydene.2024.01.045.

[14] Xu L, Xu S, Bai X-S, Repo JA, Hautala S, Hyvönen J. Performance and emission characteristics of an ammonia/diesel dual-fuel marine engine. Renew Sustain Energy Rev 2023;185:113631. https://doi.org/10.1016/j.rser.2023.113631.

[15] Chai Y, Zhang J, Zhang X, Zhang Z, Luo G, An S, Bu E. Non-isothermal kinetic study of pure-hydrogen reduction for various iron-containing raw materials. Int J Hydrogen Energy 2024;81:707–17. https://doi.org/10.1016/j.ijhydene.2024.07.172.

[16] Revolutionising steelmaking residue recycling with an innovative hydrogen-based reduction process. Available at: https://www.mecc.polimi.it/en/magazine/revolutionising-steelmaking-residue-recycling-with-an-innovative-hydrogen-based-reduction-process.

[17] Usman N, Javed A, Ullah A, Iftikhar R, Chaudhry MO. Deployment of a green hydrogen-based energy solution for the hard-to-abate steel sector. Int J Hydrogen Energy 2026;207:153540. https://doi.org/10.1016/j.ijhydene.2026.153540.

[18] Wan F, Li J, Han Y, Yao X. Research of the impact of hydrogen metallurgy technology on the reduction of the Chinese steel industry's carbon dioxide emissions. Sustainability 2024;16:1814. https://doi.org/10.3390/su16051814.

[19] Vyazovkin S, Burnham AK, Favergeon L, Koga N, Moukhina E, Pérez-Maqueda LA, Sbirrazzuoli N. ICTAC kinetics committee recommendations for analysis of multi-step kinetics. Thermochim Acta 2020;689:178597. https://doi.org/10.1016/j.tca.2020.178597.

[20] Soodmand AM, Heidari A, Zhai Y, Iljana M, Heikkilä A, Saxén H, Grénman H, Cavaliere P, Dijon L, Morais V, Fabritius T. Non-isothermal hydrogen reduction and kinetic behavior of iron ore pellets under simulated shaft furnace conditions. Metall Mater Trans B 2026. https://doi.org/10.1007/s11663-026-04051-x.

[21] Vyazovkin S, Burnham AK, Criado JM, Pérez-Maqueda LA, Popescu C, Sbirrazzuoli N. ICTAC kinetics committee recommendations for performing kinetic computations on thermal analysis data. Thermochim Acta 2011;520:1–19. https://doi.org/10.1016/j.tca.2011.03.034.

[22] Bondarchuk I, Bondarchuk S, Vorozhtsov A, Zhukov A. Advanced fitting method for the kinetic analysis of thermogravimetric data. Molecules 2023;28:424. https://doi.org/10.3390/molecules28010424.

[23] Aghili A, Shabani AH, Arabli V. Confidence interval on the activation energy obtained from differential isoconversional methods. Can J Chem Eng 2025;103:6072–82. https://doi.org/10.1002/cjce.25754.

[24] Burnham AK, Braun RL. Global kinetic analysis of complex materials. Energy Fuels 1999;13:1–22. https://doi.org/10.1021/ef9800765.

[25] Mercier Z, Carrier M, Marias F. Lumped and distributed activation energy modelling of biomass pyrolysis. Chem Eng J Adv 2026;25:100998. https://doi.org/10.1016/j.ceja.2025.100998.

[26] Dong Z, Yang Y, Cai W, He Y, Chai M, Liu B, Yu X, Banks SW, Zhang X, Bridgwater AV, Cai J. Theoretical analysis of double logistic distributed activation energy model for thermal decomposition kinetics of solid fuels. Ind Eng Chem Res 2018;57:7817–25. https://doi.org/10.1021/acs.iecr.8b01527.

[27] Cai J, Wu W, Liu R. An overview of distributed activation energy model and its application in the pyrolysis of lignocellulosic biomass. Renew Sustain Energy Rev 2014;36:236–46. https://doi.org/10.1016/j.rser.2014.04.052.

[28] Wang X, Hu Z, Mian I, Dacres OD, Li J, Wei B, Zhong M, Li X, Rahman N, Luo G, Yao H. Gasification kinetics of organic solid waste pellets: comparative study using distributed activation energy model and coats-redfern method. Energies 2022;15:9575. https://doi.org/10.3390/en15249575.

[29] Metolina P, da Silva ALN, Dixon AG, Guardani R. Multiscale modeling of non-catalytic gas-solid reactions applied to the hydrogen direct reduction of iron ore in moving-bed reactor. Int J Hydrogen Energy 2024;62:1214–30. https://doi.org/10.1016/j.ijhydene.2024.03.151.

[30] Levenspiel O. Chemical reaction engineering. Ch. 18. third ed. New York, NY, USA: John Wiley & Sons, Inc.; 1999. p. 376–402.

[31] Moreno-Pulido C, Olwande R, Myers T, Font F. Approximate solutions to the shrinking core model and their interpretation. Appl Math Model 2026;154:116715. https://doi.org/10.1016/j.apm.2025.116715.

[32] Tang Q, Ma Y, Huang K. Fe_3O_4/ZrO_2 composite as a robust chemical looping oxygen carrier: a kinetics study on the reduction process. ACS Appl Energy Mater 2021;4:7091–100. https://doi.org/10.1021/acsaem.1c01152.

[33] Liu L, Guo Q-X. Isokinetic relationship, isoequilibrium relationship, and enthalpy-entropy compensation. Chem Rev 2001;101:673–96. https://doi.org/10.1021/cr9904162.

[34] Eyring H. The activated complex in chemical reactions. J Chem Phys 1935;3:107–15. https://doi.org/10.1063/1.1749604.

[35] Mianowski A, Radko T, Bigda R. Isokinetic and compensation temperature in the analysis of thermal dissociation of the solid phase under dynamic conditions. Energies 2023;16:5692. https://doi.org/10.3390/en16155692.

[36] Dang J, Chou K-C, Hu X-J, Zhang G-H. Reduction kinetics of metal oxides by hydrogen. Steel Res Int 2013;84:526–33. https://doi.org/10.1002/srin.201200242.

[37] Luo Y, Shi Y, Li W, Cai N. Mechanism of rate-limiting step switchover for reversible solid oxide cells in H_2/H_2O atmosphere. Electrochim Acta 2019;326:135003. https://doi.org/10.1016/j.electacta.2019.135003.

[38] Vyazovkin S, Wight CA. Model-free and model-fitting approaches to kinetic analysis of isothermal and nonisothermal data. Thermochim Acta 1999;340–341:53–68. https://doi.org/10.1016/S0040-6031(99)00253-1.

[39] Pineau A, Kanari N, Gaballah I. Kinetics of reduction of iron oxides by H_2: part I: low temperature reduction of hematite. Thermochim Acta 2006;447:89–100. https://doi.org/10.1016/j.tca.2005.10.004.

[40] Villarroel-Rocha J, Gil A. Modeling the temperature-programmed reduction of metal oxide catalysts by considering the particle-size distribution effect. Chem Eng J 2024;487:150722. https://doi.org/10.1016/j.cej.2024.150722.

[41] Artiaga R, Cao R, Naya S, González-Martin B, Mier JL, Garcia A. Separation of overlapping processes from TGA data and verification by EGA. In: Pan W-P, Judovits L, editors. Techniques in thermal analysis: hyphenated techniques, thermal analysis of the surface, and fast rate analysis, 12. ASTM International, Volume: STP1466-EB, Conference: ASTM Special Technical Publication; 2007. https://doi.org/10.1520/STP45226S.

[42] Galwey AK, Brown ME. In: Thermal decomposition of ionic solids - chemical properties and reactivities of ionic crystalline phases. first ed., 86. Amsterdam, The Netherlands: Elsevier; 1999. ISBN: 9780444824370.

[43] Spreitzer D, Schenk J. Reduction of iron oxides with hydrogen - a review. Steel Res Int 2019;90:1900108. https://doi.org/10.1002/srin.201900108.

[44] Heidari A, Niknahad N, Iljana M, Fabritius T. A review on the kinetics of iron ore reduction by hydrogen. Materials 2021;14:7540. https://doi.org/10.3390/ma14247540.

[45] Sohn HY, Szekely J. A structural model for gas-solid reactions with a moving boundary - IV. langmuir-hinshelwood kinetics. Chem Eng Sci 1973;28:1169–77. https://doi.org/10.1016/0009-2509(73)85026-2.

[46] Si J, Su F. Multistep kinetics study on hydrogen reduction of 0.25-0.5 mm iron oxide particles. Processes 2025;13:893. https://doi.org/10.3390/pr13030893.

[47] Dang J, Wu Y, Lv Z, You Z, Zhang S, Lv X. A new kinetic model for hydrogen reduction of metal oxides under external gas diffusion controlling condition. Int J Refract Hard Met 2018;77:90–6. https://doi.org/10.1016/j.ijrmhm.2018.07.011.

[48] D'Angelo A, Salucci E, Russo V, Grénman H, Saxén H. Hydrogen reduction of iron oxide powder in thin layers. Ind Eng Chem Res 2025;64:158–70. https://doi.org/10.1021/acs.iecr.4c03138.

[49] Zhang H, Li Z, Yang Y, Zha G, Xu B, Liu D, Yang B, Jiang W. Advances in tellurium recovery and purification: a comprehensive review of separation methods and emerging technologies. Resour Conserv Recycl 2025;215:108160. https://doi.org/10.1016/j.resconrec.2025.108160.

[50] Juillet C, Auzoux Q, Datcharry F, Martin F, Tupin M. Kinetics of deuterium permeation through Zircaloy-4 in the 623-773 K temperature range. Int J Hydrogen Energy 2021;46:25860–70. https://doi.org/10.1016/j.ijhydene.2021.05.093.

[51] Wang H, Liu B, Yang G, You C. Multistep kinetic study of Fe_2O_3 reduction by H_2 based on isothermal thermogravimetric analysis data deconvolution. Int J Hydrogen Energy 2023;48:16601–13. https://doi.org/10.1016/j.ijhydene.2023.01.201.

[52] Lu X, Xu Q, Kang H, Shi J, Cao Z, Chen B, Guo L. Multistep kinetic study of magnetite reduction by hydrogen based on thermogravimetric analysis. Int J Hydrogen Energy 2024;73:695–707. https://doi.org/10.1016/j.ijhydene.2024.06.081.

[53] Chen Z, Dang J, Hu X, Yan H. Reduction kinetics of hematite powder in hydrogen atmosphere at moderate temperatures. Metals 2018;8:751. https://doi.org/10.3390/met8100751.

[54] Marsigny A, Letz J-B, Mirgaux O, Patisson F. Kinetics of the reduction of iron ore pellets with hydrogen: a parametric experimental and modeling study. Metals 2025;15:1034. https://doi.org/10.3390/met15091034.

[55] Hidayat T, Rhamdhani MA, Jak E, Hayes PC. The kinetics of reduction of dense synthetic nickel oxide in H_2-N_2 and H_2-H_2O atmospheres. Metall Mater Trans B 2009;40:1–16. https://doi.org/10.1007/s11663-008-9212-0.

[56] Tilliander U, Aune RE, Seetharaman S. Kinetics studies of hydrogen reduction of Cu_2O. Int J Mater Res 2006;97:72–8. https://doi.org/10.1515/ijmr-2006-0011.
[57] Numazawa Y, Hara Y, Matsukawa Y, Matsushita Y, Aoki H, Shishido T, Okuyama N. Kinetic modeling of CO_2 and H_2O gasification reactions for metallurgical coke using a distributed activation energy model. ACS Omega 2021; 6:11436–46. https://doi.org/10.1021/acsomega.1c00443.
[58] Sohn HY, Wadsworth ME. Rate processes of extractive metallurgy. New York, USA: Plenum Press; 1979. https://doi.org/10.1007/978-1-4684-9117-3. ISBN-13: 978-0-306-31102-4.
[59] Šesták J, Berggren G. Study of the kinetics of the mechanism of solid-state reactions at increasing temperatures. Thermochim Acta 1971;3:1–12. https://doi.org/10.1016/0040-6031(71)85051-7.
[60] Yelon A, Movaghar B, Branz HM. Origin and consequences of the compensation (Meyer-Neldel) law. Phys Rev B 1992;46:12244. https://doi.org/10.1103/PhysRevB.46.12244.
[61] Exner O. On the enthalpy-entropy-relationship. Collect Czech Chem Commun 1964;29:1094–113. https://doi.org/10.1135/cccc19641094.
[62] Krug RR, Hunter WG, Grieger RA. Enthalpy-entropy compensation. 1. Some fundamental statistical problems associated with the analysis of van't hoff and arrhenius data. J Phys Chem 1976;80:2335–41. https://doi.org/10.1021/j100562a006.